**Key Points:**
- A high-resolution inner-shelf mooring array reveals headland influence in subtidal, diurnal, and semidiurnal temperature ($T$) variability
- Diurnal-$T$ variability is not wind forced, varies with headlands, and though subcritical, propagates alongshore in nonheadland regions
- Semidiurnal-$T$ variability is most complex, with strong interrelated vertical and alongshore variability that is headland influenced

**Correspondence to:**
J. H. MacMahan,
jhmacmah@nps.edu

# Inner-Shelf Vertical and Alongshore temperature Variability in the Subtidal, Diurnal, and Semidiurnal Bands Along the central California coastline with headlands

**Falk Feddersen[1]** [iD], **Jamie H. MacMahan[2]** [iD], **Thomas M. Freismuth[2]** [iD], **Matt K. Gough[2]**, and **Michael Kovatch[1]** [iD]

[1]Scripps Institution of Oceanography, University of California, San Diego, CA, USA, [2]Department of Oceanography, Naval Postgraduate School, Monterey, CA, USA

**Abstract** The temporal, vertical, and alongshore variation in inner-shelf temperature, $T$, across subtidal (ST), diurnal (DU), and semidiurnal (SD) bands on coastlines with headlands is not understood. Inner-shelf $T$ was observed with 20 moorings in 9- to 16-m depth with high vertical density during Fall 2017 along 50 km of central California coastline with headlands. The ST-first empirical orthogonal function is largely barotropic. ST warm water events are associated with northward-propagating buoyant plumes and onshore advection of offshore water, with headland effects, particularly for stronger events. Previous plume arrival criteria are northward propagation biased. The DU vertical structure was mixed barotropic and linear baroclinic, without surface extrema. Inner-shelf DU-band temperature variability was always evident, largest north of and weakest south of two headlands. The DU-$T$ envelope was not modulated by ST stratification and was not linked to the modeled DU-wind envelope. North of one headland, the alongshore first complex empirical orthogonal function of DU temperature has a previously unobserved southward 2-m/s phase propagation, even though DU frequency is subcritical, that is, not wind forced. A frictional subcritical wave mechanism is proposed for the DU propagation. The SD-$T$ vertical structure varies alongshore, suggesting at different locations linear internal waves and nonlinear cold bores. SD-$T$ variability was incoherent with barotropic tides and decorrelates alongshore in 7.5 km, contrasting with a few kilometers offshore. The SD depth-averaged energy varied strongly alongshore particularly north and south of the headlands, and stronger and weaker SD energy was linked to nonlinear and linear baroclinic vertical structures, respectively, which are headland influenced.

**Plain Language Summary** How water temperature ($T$) varies both in the vertical, along the coast, and in time at both tidal and longer time scales has important implications in the distribution, retention, and settlement of marine biota and nutrients. Temperature variability in regions near coastal headlands is not understood. Twenty inner-shelf moorings with a high vertical number of temperature sensors were deployed in 9- to 16-m water depths along 50 km of the central California inner shelf to measure temporal, vertical, and alongshore $T$ variability. At 36 hr or longer time scales, water temperature varies due to warm plumes that propagate northward or onshore that are affected by the headlands. Water temperature always varies on a daily cycle; however, this variation is not due to daily solar heating or to daily sea breezes. Instead, daily $T$ variability propagates like a wave alongcoast, in a manner inconsistent with theory, and a new mechanism is proposed to explain the propagation. The twice-daily $T$ variability has vertical structure that varies strongly along the coast, suggesting different types of internal wave processes. The twice-daily $T$ variation was not directly related to the tides and decorrelates rapidly along the coast, counter to previous observations made a few kilometers farther offshore.

## 1. Introduction

Inner-shelf water temperatures can significantly vary spatially and temporally (e.g., Aristizabal et al., 2016, 2017; Boehm et al., 2004; Tapia et al., 2014). Here, the inner shelf is geographically defined as seaward of the surf zone, where depth-limited wave breaking occurs, out to about 20-m water depth. The inner-shelf water temperature ($T$) variability has important implications in the distribution, retention, and settlement of marine biota (O'Connor et al., 2007; Tapia et al., 2014), the delivery of nutrients

(Lucas et al., 2011; McPhee-Shaw et al., 2007), and can be a measure of cross-shore exchange (Hally-Rosendahl et al., 2014).

Studies of inner-shelf $T$ variability can be divided into two general categories: (1) heat budgets and (2) statistical analyses. A heat budget accounts for the total heat change of a control volume due to cross-shore, along-shore, and surface heat fluxes. Heat budgets have identified how processes such as upwelling-, internal waves-, and sea breeze-driven transport contribute to inner-shelf water $T$ variability at subtidal (ST, $f < 33^{-1}$ cph; Austin, 1999; Fewings & Lentz, 2011), diurnal (DU, $33^{-1} < f < 16^{-1}$ cph; Herdman et al., 2015; Molina et al., 2014; Suanda et al., 2011), and semidiurnal (SD, $16^{-1} < f < 10^{-1}$ cph; Sinnett & Feddersen, 2019) time scales. Estimates of cross-shore and alongshore heat fluxes require colocated measures of water $T$ and currents over the vertical as well as adequate alongshore spacing to identify advective heat flux divergences (e.g., Austin, 1999), which can develop from coastal inhomogeneities, such as coastal topography or kelp forests (Suanda et al., 2011). Thus, heat budget studies are impractical over long stretches of inhomogeneous coastlines.

Statistical analysis of the temporal, vertical, and alongshore $T$ (co) variability can link magnitudes and scales of variability to processes and the effects of coastal heterogeneity such as headlands. In addition, $T$ variability is explored across different frequency bands (e.g., ST, DU, or SD) that differ in forcing and scale. For example, along 800 km of the central Chilean coast, nearshore ST-band $T$ variability was related to the alongshore wind stress (i.e., upwelling and downwelling) and to coastal headlands (Tapia et al., 2014). On the central California coast, ST-band $T$ variability is primarily associated with northward-propagating warm, buoyant (density changes $\Delta\rho$ of 0.1–0.8 kg m$^{-3}$) plumes originating from the Santa Barbara Channel (SBC), associated with wind relaxation events (Melton et al., 2009; Washburn et al., 2011). These warm buoyant plumes have been in situ observed to propagate to San Simeon, CA, where the propagation distance increases with duration of wind relaxation (Melton et al., 2009). Washburn et al. (2011) observed up to 4 °C plume to ambient water temperature differences with propagation speeds between 15–30 km day$^{-1}$. The ST warm plumes tend to occupy the entire water column on the inner shelf (Suanda et al., 2016; Washburn et al., 2011) and have been interpreted using a two-fluid gravity current on an alongshore uniform slope theory (Lentz & Helfrich, 2002). In addition, intrusions of offshore SBC-origin warm water onto the inner shelf have also been observed north of Pt. Conception (Nidzieko & Largier, 2013). The changes in stratification induced by these warm plumes have been observed to modulate both the DU- and SD-$T$ fluctuations (Aristizabal et al., 2017).

Inner-shelf DU-$T$ variability can be related to a number of concomitant processes, such as direct wind forcing (e.g., Kaplan et al., 2003), DU heating (e.g., Molina et al., 2014), and resonant forcing (e.g., Nam & Send, 2013). In the northern and southern portions of the SBC, near-bottom DU-$T$ and DU winds were coherent with no phase lag, suggesting direct wind forcing without any alongshore propagation (Aristizabal et al., 2016). DU winds can also induce local coastal upwelling along coastal headlands (e.g., Suanda et al., 2011; Woodson et al., 2007) or in coastal embayments (Walter et al., 2017). DU winds can also drive baroclinic (internal) modal oscillations that can be resonant when ST shear reduces the effective Coriolis parameter (Kumar et al., 2016; Lerczak et al., 2001; Nam & Send, 2013) or when the inertial and DU periods align (e.g., Lucas et al., 2014). DU internal motions have amplitudes that increase with larger background stratification (Cudaback & McPhee-Shaw, 2009). At some SBC near-bottom locations, DU-$T$ variability can be linked to the barotropic tide (Aristizabal et al., 2016).

Inner-shelf SD-$T$ variability often is influenced by internal waves (e.g., Pineda & Lopez, 2002). SD-band near-bed $T$ variability was elevated on the mainland (north) SBC and decreased north of Pt. Conception, CA (Aristizabal et al., 2016). This SD-band variability was incoherent alongshore (Aristizabal et al., 2016) and presumably incoherent with the barotropic tide. However, at locations near Santa Cruz island, SD-band near-bed $T$ variability was coherent due to the proximity to an SD, internal-tide generation region (Aristizabal et al., 2016). Similarly, in a 6-km wide Chilean bay in 20-m depth, the SD-$T$ variability was coherent across the bay and with the barotropic tide (Bonicelli et al., 2014), likely due to proximity to a submarine canyon as a source region. Just offshore of Pt. Sal, CA, during summer 2015, Colosi et al. (2018) observed nonlinear internal waves with significant energy in the SD-band from 50- to 20-m water depth. In 50-m depth, the SD internal tide was relatively alongshore uniform north and south of Pt. Sal and was

approximately one half coherent with the barotropic tide (Kumar et al., 2019). Modeling suggests the SD internal tide is generated at least a few 100 km offshore (Kumar et al., 2019).

Previous statistical temperature studies that described inner-shelf $T$ variability over long-durations (O(10 years)) were limited in mooring number or the total thermistors resulting in poor vertical or alongshore spatial resolution. For example, Tapia et al. (2014) had a single thermistor at 15 locations spanning 800 km, with 50-km typical spacing. Previous Santa Maria Basin (SMB) $T$ observations also spanned multiple years but were limited to a few locations on the south side of the topographic points, resulting in an alongshore mooring spacing of $\geq$ 17 km and did not extend north of Pt. Sal (Aristizabal et al., 2016, 2017; Cudaback & McPhee-Shaw, 2009; Melton et al., 2009; Washburn et al., 2011). Furthermore, the 15-m depth $T$ moorings were composed of three thermistors sensors located near the bottom, middle, and surface resulting in relatively coarse (~5 m) vertical resolution. Some analyses used only the near-bed thermistor. Thus, alongshore and vertical variation in inner-shelf $T$ variability near alongshore heterogeneous coastlines (such as Pt. Sal, CA) across different frequency bands is not known, as well as their linkage to processes such as the winds and onshore-propagating SD internal tide.

Here, inner-shelf temperature observations are analyzed that are part of the 2017 Inner Shelf Dynamics Experiment (Lerczak et al., 2019) data set. Inner-shelf temperature observations were collected over 1.5 months along 50 km of the heterogeneous SMB region north and south of Pt. Sal, CA, from 20 moorings with high vertical resolution in 9- to 16-m water depth (Figure 1). Herein, a statistical analysis is performed with these observations to describe the vertical, alongshore, and temporal variability in the ST, DU, and SD bands and link to the processes driving variability. The observations and the empirical orthogonal function (EOF)-based methodology are given in section 2. The vertical, alongshore, and temporal $T$ variability in the ST, DU, and SD bands is described in section 3. The variability of each band is contextualized in the section 4, and section 5 provides a summary.

## 2. Methods

### 2.1. Study Region

This study utilizes a subset of the Inner Shelf Dynamics Experiment data (e.g., Lerczak et al., 2019; McSweeney et al., 2019). The study site is within the SMB along the central California coast (Figure 1a) with coastline characterized by a headland-and-straight coastline topography with three rocky headlands (or topographic points): Pt. Sal (34.9°N), Pt. Purisima (34.76°N), and Pt. Arguello (34.58°N). Note that Pt. San Luis (35.26°N) to north of experimental site also influences the observations. The 10–20 km of coastlines located north of the three headlands are generally oriented ≈15° east of north (Figure 1b). The coastlines located to the south of the headlands are oriented ≈30° west of north for approximately 6–8 km (Figure 1b). In addition to the larger headland features, a small (~0.3 km) headland Mussel Pt. (34.93°N) with a subaqueous rocky outcrop 2 km offshore (Figure 1c) is located 3 km north of Pt. Sal. Another small headland is located 3.5 km south of Pt. Sal. Of note, San Luis Obispo (SLO) Bay is located at 35.17°N.

### 2.2. Temperature Observations, Measured Winds, and Modeled Winds

Measures of temperature, $T(y,z,t)$, were obtained over the vertical ($z$) at 20 temperature-string moorings (denoted M1 to M20; Figure 1b) deployed in an alongshore array ($y$) on the inner shelf from SLO Bay to Pt. Arguello, California, for Yeardays 244–287 (1 September to 14 October 2017). The N-S spacing between moorings ranged from 670 m to 50 km. A total of 15 moorings were deployed along the 9-m isobath (M1–M5 and M11–M20). For 9-m moorings, thermistors were located from 1.5 m above the seabed to mean low low-water (MLLW) with a vertical resolution of 0.5 m. Five moorings located near Pt. Sal (M6–M10; Figure 1b) were deployed in 10- to 16-m water depths and obtained $T$ from 0.5 m above the seabed to MLLW with 1.5-m vertical resolution. A subsurface float was located below MLLW so that the $T$ mooring remained nearly vertical over the $\pm$1-m tidal range. All thermistors were RBRsolo T and sampled at 1 s. For analysis, data were averaged to 10 min. Winds were obtained hourly at four locations throughout the experiment site (Figure 1b; denoted at W1–W4). W1 is an offshore mooring site. Locations W2 and W4 are located very close to shore, and W3 is moored in 20-m depth. Modeled 10-m winds from a 2-km horizontal resolution Coupled Ocean/Atmosphere Mesoscale Prediction System (COAMPS) forecast model (Hodur, 1997) were linearly interpolated in three dimensions (longitude, latitude, and time) to the $T$ mooring locations. The easting and northing wind velocities $u_e$ and $u_n$ are defined in the toward direction.
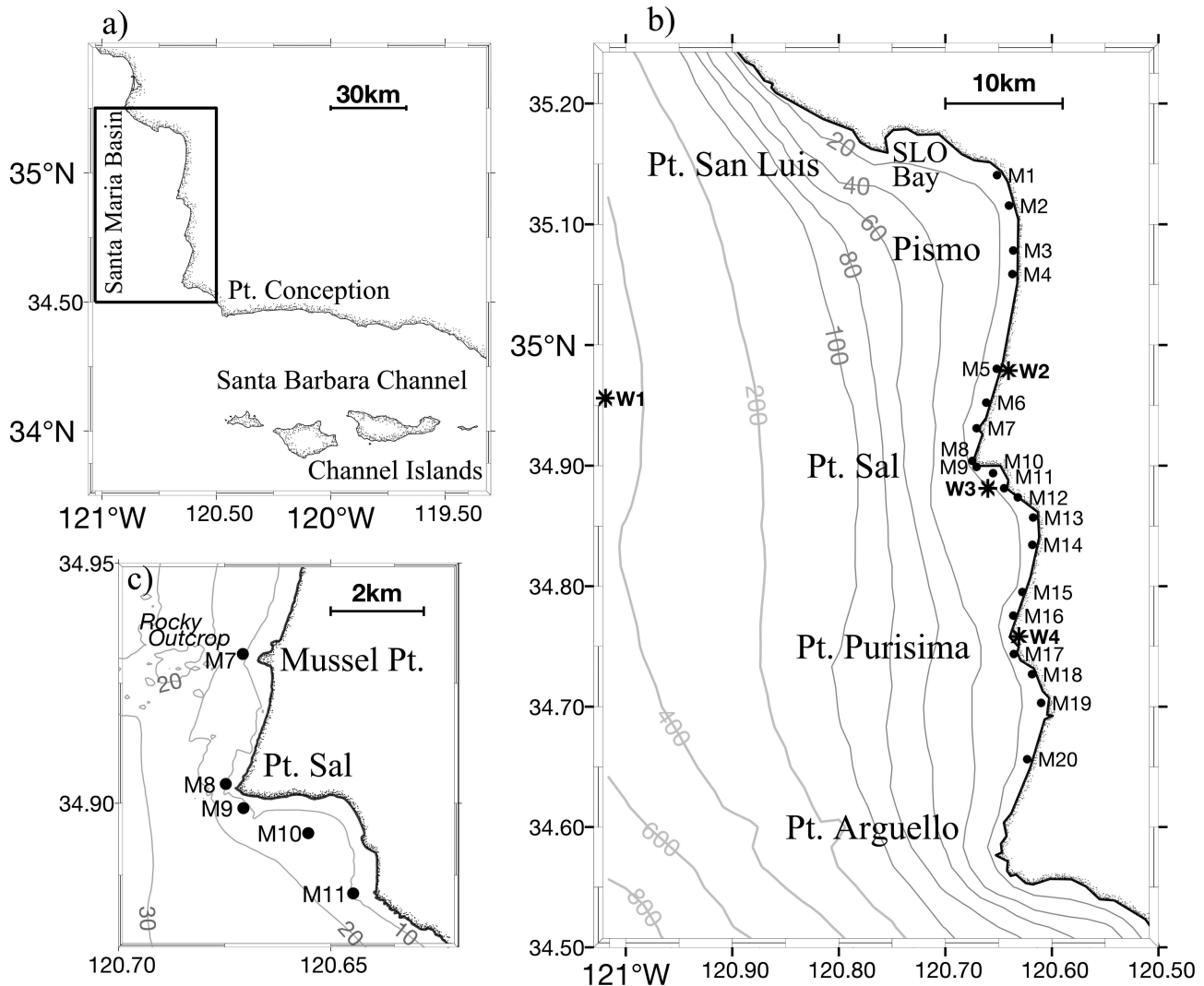
**Figure 1.** (a) Map of the Santa Maria Basin in context with the Santa Barbara Channel and Pt. Conception. Overview of the study region highlighted with a black box, which is shown in (b). (b) Map of the experiment site. (c) Map of Pt. Sal. Temperature mooring positions are indicated by black dots with given mooring ID. Location of wind observations are indicated by black asterisks. Depth contours are depicted as gray lines.

### 2.3. Temperature Filtering, Vertical EOF Analysis, and Identification of Warm Plume Arrival Times

At each thermistor on each mooring, temperature $T(z,t)$ was decomposed into a mean $T$ and four frequency bands, ST ($<33^{-1}$ cph, $T^{(ST)}(z,t)$), DU ($33^{-1}$ to $16^{-1}$ cph, $T^{(DU)}(z,t)$), SD ($16^{-1}$ to $10^{-1}$ cph, $T^{(SD)}(z,t)$), and high frequency ($>10^{-1}$ cph, not considered) with a frequency domain filter. Note the parenthetical superscript represents the frequency band of interest (i.e., ST, DU, and SD). Owing to differences in mooring water depths and thermistor vertical locations $z$, vertical locations are depth ($h$) normalized, where $z/h = 0$ represents the sea surface and $z/h = -1$ represents the ocean bottom. Normalizing thermistor $z$ location by mean (tidally averaged) water depth as opposed to tidally varying water depth induces a small aliasing. At each mooring, the shape of the vertical $T$ profile is isolated by a normalized mean temperature $\widetilde{T}(z/h)$, defined as

$$\widetilde{T}\left(\frac{z}{h}\right) = \frac{T - T_b}{T_s - T_b}, \tag{1}$$

where $T_b$ and $T_s$ are the mean near-bed and near-surface mean $T$, respectively, and the mean is a time average over the experiment duration. Thus $\widetilde{T} = 0$ at the bed and $\widetilde{T} = 1$ at the surface. At each mooring, the

dominant coherent vertical variability of $T$ in each band $T^{(\text{band})}(z/h,t)$, where "band" is ST, DU, or SD, is decomposed into vertical EOFs (eigenfunctions), $\phi_n^{(\text{band})}(s/h)$, and time-varying amplitudes, $A_n^{(\text{band})}(t)$, referred to as principal components (Preisendorfer, 1988). Variability is separated into orthogonal modes, such that (for the ST band)

$$T^{(\text{ST})}(z/h, t) = \sum_{n=1}^{N} A_n^{(\text{ST})}(t)\phi_n^{(\text{ST})}(z/h) \,, \tag{2}$$

where $T^{(\text{ST})}(z/h,t)$ is the ST temperature, $N$ is the total number of measurements over the vertical, and the first mode ($n = 1$) describes the largest fraction of variance. For evaluating vertical structure across all moorings, the first EOF mode vertical structure, $\phi_1^{(\text{band})}(z/h)$ is normalized in all three bands such that

$$\int_{-1}^{0} \left[\phi_1^{(\text{band})}(z/h)\right]^2 d(z/h) = 1. \tag{3}$$

Lastly, the arrival time of SBC-origin warm plumes are identified using the method of Melton et al. (2009) as described here. At each mooring, the first EOF reconstructed near-surface ST $T$ (2) time derivative is estimated using 0.1667-hr (10 min) differences. At each mooring, the arrival time of a warm plume, $t_{\text{plume}}$, is defined to be the time of maximum near-surface $dT^{(\text{ST})}/dt$ exceeding 0.031 °C hr$^{-1}$. Melton et al. (2009) imposed an additional criterion that requires $t_{\text{plume}}$ at a subsequent northern mooring must occur after its closest subsequent southern mooring. The temperature at the arrival time is denoted as $T_{\text{plume}}$. The arrival times are differenced by arrival time at the southernmost mooring, for example, $\Delta t_{\text{plume}}(y) = t_{\text{plume}}(y) - t_{\text{plume}}(y_{\text{M20}})$, where $y_{\text{M20}}$ indicates the southernmost mooring (M20) location. In addition to the Melton et al. (2009) $t_{\text{plume}}$ statistic, we also identify the maximum warm-plume temperature, $T_{\text{max}}$, as the maximum temperature within 72 hr of $t_{\text{plume}}$, which is also reported relative to M20, $\Delta T_{\text{max}}(y) = T_{\text{max}}(y) - T_{\text{max}}(y_{\text{M20}})$. The time of $T_{\text{max}}$ is similarly denoted as $t_{\text{max}}$ and is given as relative to $t_{\text{max}}$ at M20, $\Delta t_{\text{max}}(y) = t_{\text{max}}(y) - t_{\text{max}}(y_{\text{M20}})$.

## 3. Results

### 3.1. Coastal Winds

The Fall 2017-modeled (COAMPS) wind patterns are consistent with previous wind observations in this region (e.g., Fewings et al., 2015; Melton et al., 2009; Ohashi & Wang, 2004). The easting winds, $u_e$, are dominated by persistent DU variability and some ST synoptic variability that is relatively consistent across latitude with weakening just south of the Pt. Sal (Figure 2a). The northing (or poleward) winds, $u_n$, are weaker than $u_e$ with both DU and ST variability (Figure 2b). Upwelling favorable southward ST $u_n$ events (blue colors in Figure 2b) persist for 3–7 days and are relatively coherent across latitude from 35.05 N to the south. Relaxations or reversal events with northward $u_n$ winds (e.g., Melton et al., 2009; Washburn et al., 2011) also occur (green-yellow colors in Figure 2b). The COAMPS-modeled winds have variances that are similar to the observed winds (Figure 3a). The observed and modeled easting winds, $u_e$, have zero-lag correlation coefficients >0.5 (circles in Figure 3b). The observed and modeled northing winds, $u_n$, are also similarly correlated except at W2 ($r = 0.35$; squares in Figure 3a). The similarity between model and observations indicate that using modeled winds at mooring locations is appropriate.

### 3.2. Vertical Water Temperature $T(z,t)$ at Mooring 15 (M15)

An example of the M15 (at 34.78°N located between Pt. Sal and Pt. Purisima) $T(z,t)$ highlights the vertical and temporal variability (Figure 4) along the 50-km N-S array. The observed $T(z,t)$ reveals a range of vertical and temporal variability (Figure 4a). The mean and ST-$T$ variability (Figure 4b) is characterized by colder water (<14 °C) upwelling events and warmer water (>15 °C) plume events (e.g., Yeardays 246–260). The DU-$T$ variability $T^{(\text{DU})}(z,t)$ occurs throughout the water column and is $\pm1.0$ °C (Figure 4c), with larger fluctuations occurring earlier in the experiment with intermittent events occurring later in the experiment. The SD-$T$ $T^{(\text{SD})}(z,t)$ also varies $\pm1.0$ °C and is largest midwater column, with strongest variability occurring earlier in the experiment (Figure 4d). Hourly tidal elevation is provided for context in Figure 4e. The tidal fluctuations on the West Coast of the Unite States are described by a mixed, SD tide with a range of $\pm1$ m, where the higher-high water precedes lower-low water (Friedrichs, 1995). The tidal amplitude is modulated by
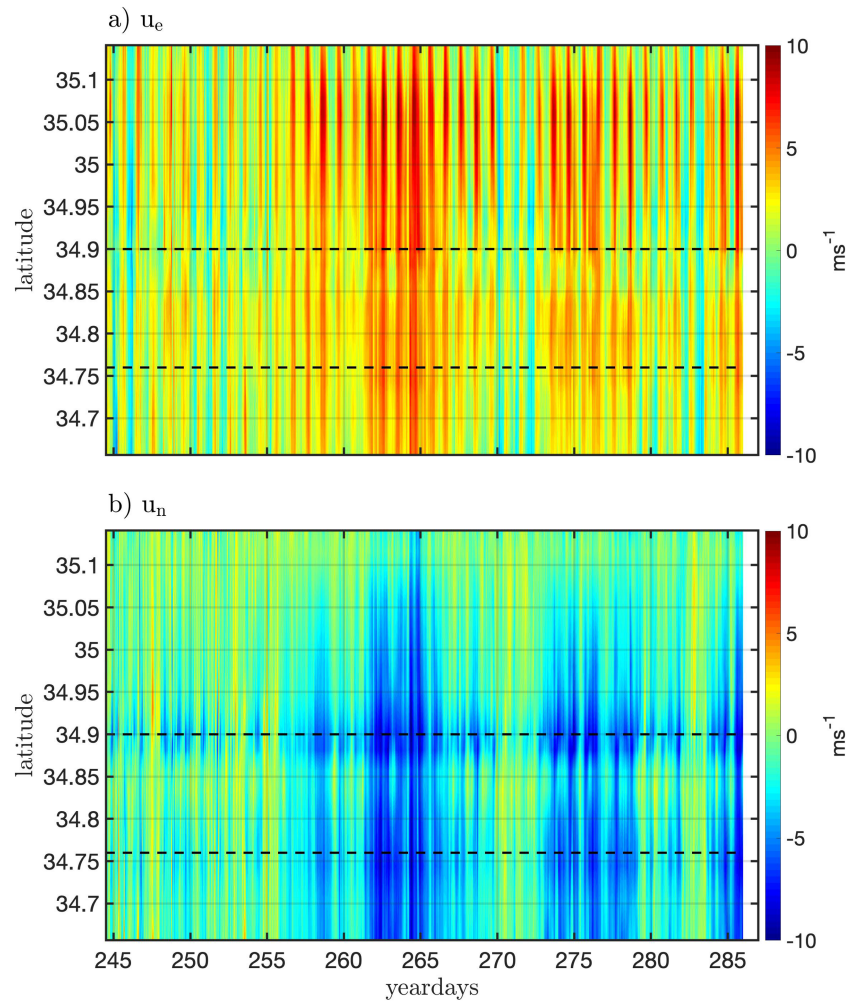
**Figure 2.** Hovmoller diagrams of spatially interpolated to mooring locations (Figure 1b) COAMPS-modeled (a) easting winds, $u_e$, and (b) northing, $u_n$, wind velocities as a function of latitude and yearday. Horizontal dashed black lines indicate the locations of Pt. Sal and Purisima. The color scale represents wind velocity.
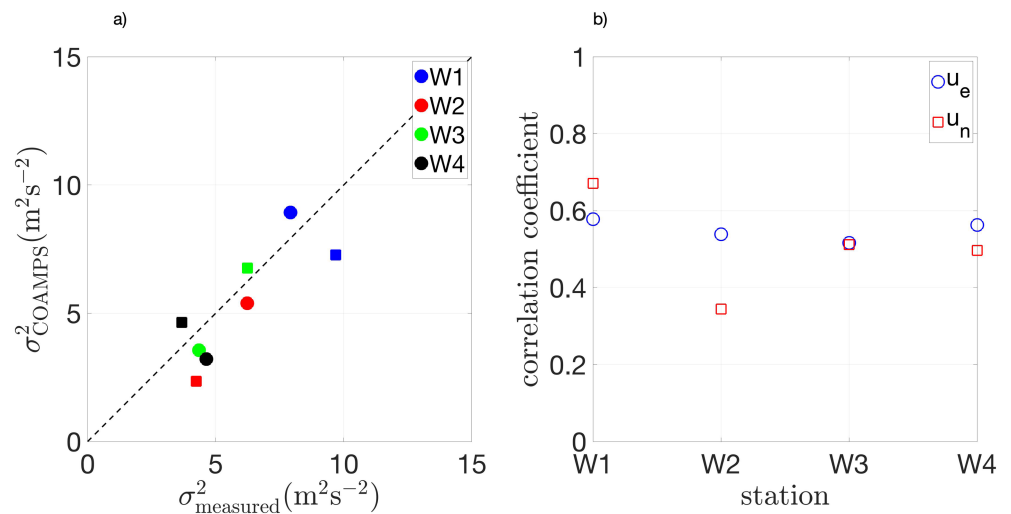


**Figure 3.** COAMPS modeled (Figure 2) and observed W1–W4 (Figure 1b) comparison for $u_e$ (circles) and $u_n$ (squares) (a) modeled versus observed wind variance with station location colored (see legend) and (b) correlation coefficient versus station location. Black dashed line represents the linear 1:1 line.
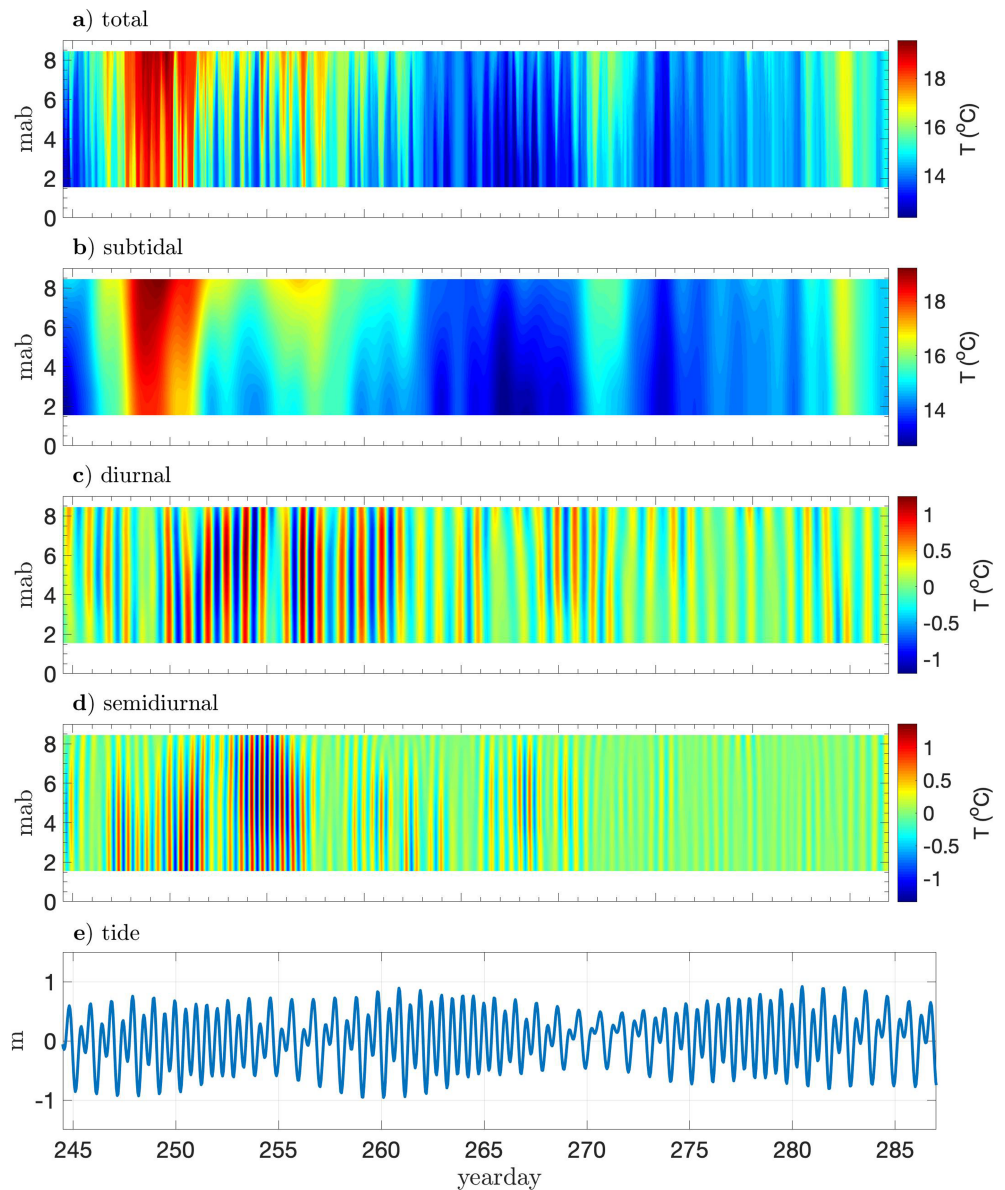
**Figure 4.** Temperature observations versus 2017 yearday and height above the bed at M15 for the (a) total, (b) subtidal, (c) diurnal, and (d) semidiurnal frequency bands (see Figure 1b). (e) Tidal elevations versus 2017 yearday.

lunar (K1) and lunisolar (O1) DU tides with principal lunar SD tide (M2) (Godin & Martínez, 1994; Nidzieko, 2010) with maxima of the spring tides occurring around Yeardays 284, 261, and 282 (Figure 4e).

### 3.3. Midwater Column Temperature Spectra at M1 and M7

Temperature spectra with 10 DOF and frequency resolution of 0.002 cph were computed in the midwater column $(z = -4 \text{ m})$ at two contrasting sites: M1 (35.14°N) to the north near SLO Bay and M7 (34.91°N) at Mussel Pt. near Pt. Sal (Figure 5). At low frequencies in the ST band, the spectral energy is red with similar levels at M1 and M7. The ST band contributes 68% (M1) and 48% (M7) of the total $T$ variance. At both M1 and M7, the DU and SD spectral peaks are similar per mooring. The DU and SD spectra peaks are broad and not at distinct tidal frequencies. DU and SD spectral levels are elevated at M7, which has 3× more variance than at M1. Spectra levels decrease in the high frequency band (>0.1 cph), and no clear harmonic of the SD internal tide is seen. This contrasts with the twice an SD period nonlinear internal bore arrivals offshore of M5
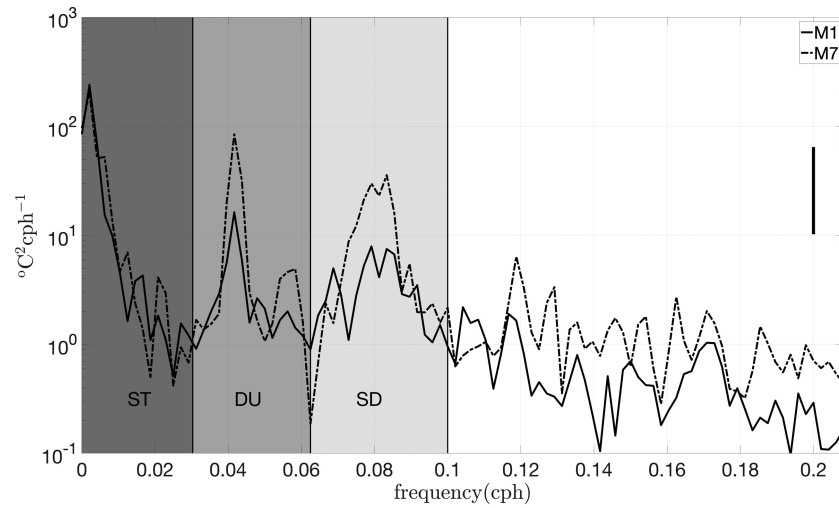
**Figure 5.** Midwater column (at $z = -4.0$ m) temperature spectra versus frequency (in cycles per hour [cph]) at M1 (solid) and M7 (dashed). The subtidal (ST), diurnal (DU), and semidiurnal (SD) bands are indicated. Spectra were computed using 6-day hamming window with 50% overlap resulting in 10 DOF and 0.002 cph frequency resolution. Thick vertical black line in the right-hand side represents the 95% confidence levels.

(McSweeney et al., 2019). The spectral valleys between peaks are used to define the ST, DU, and SD band cutoffs (section 2.3).

### 3.4. Vertical Temperature Statistics: Mean and ST, DU, and SD EOFs

Across all moorings, the normalized mean temperature $\widetilde{T}(z/h)$ profile (1) has a largely linear vertical structure with some midwater column variation (Figure 6a). The mean (time averaged) stratification $N^2$ is estimated solely from the time-averaged $T$ profiles (assuming salinity effects are weak) as

$$N^2 = -\frac{g\alpha}{\rho_o}\frac{\partial T(z)}{\partial z}, \tag{4}$$

where $g$ is gravity, $\rho_o = 1{,}025$ kg m$^{-3}$, $\alpha$ is the thermal expansion coefficient, and the mean $T$ gradient is from the linear mean $T$ profile (Figure 6a). The linear $\widetilde{T}(z/h)$ profiles suggest that the time-averaged mean stratification $N^2$ is largely depth uniform across all moorings. In the ST band, the first EOF represents between 95% to 99% of the variance, and across all moorings, the $\phi_1^{(ST)}(z/h)$ vertical structure is near 1 and mostly depth uniform (Figure 6b), consistent with a largely barotropic response. However, the mooring averaged $\phi_1^{(ST)}(z/h)$ does have some vertical structure, varying by 0.18 top to bottom, which impacts the ST stratification. The $\phi_1^{(ST)}(z/h)$ variability across moorings is weak, suggesting that the ST vertical variability can be well represented by a single mode across all moorings.

In the DU band, the first EOF represents 75% to 95% (mean 87%) of the variance. Across all moorings, the mean vertical structure of $\phi_1^{(DU)}(z/h)$ has a weak midwater column maximum with near-surface and near-bed minima that are two thirds of the maximum (Figure 6c), indicating a mixed barotropic and first mode baroclinic response. The $\phi_1^{(DU)}(z/h)$ is consistent with the DU temperature structure observed in 8-m and 10-m depth off of Huntington Beach, CA (Kumar et al., 2016). The weaker near-surface first EOF $\phi_1^{(DU)}(z/h)$ indicates that surface heating and cooling are not dominant in forcing DU variability. Across all moorings, the $\phi_1^{(DU)}(z/h)$ variability is weak midwater column that increases slightly near surface and near bed (dashed lines in Figure 6c), also suggesting that a single mode largely can represent the DU-vertical variability across all moorings.

In the SD band, the first EOF represents 76% to 95% (mean of 88%). Across all moorings, the mean $\phi_1^{(SD)}(z/h)$ vertical structure has a clear Mode 1-like baroclinic response, although $\phi_1^{(SD)}(z/h)$ is maximum in the
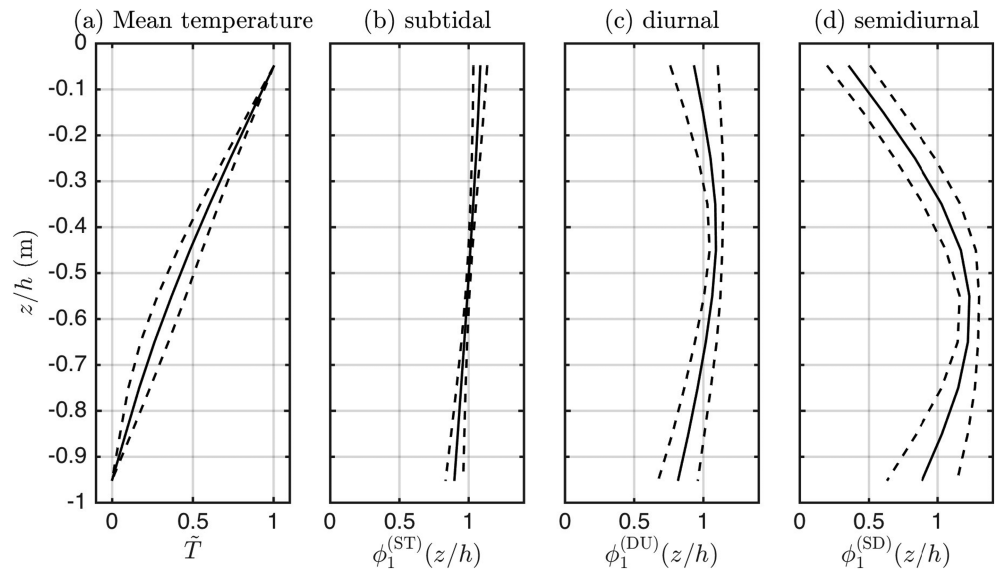
**Figure 6.** The mean (solid lines) and ± standard deviations (dashed) of temperature statistics across all 20 moorings as a function of normalized depth $z/h$: (a) normalized time mean temperature $\widetilde{T}(z/h)$ (1) and normalized first EOF $\phi_1$ $(z/h)$ for the (b) subtidal, (c) diurnal, and (d) semidiurnal frequency band. The moorings span a depth range of 9 to 16 m (Figure 1a).

lower-mid ($z/h = -0.65$) water column with asymmetric response above and below (Figure 6d). Similar $\phi_1^{(SD)}$ $(z/h)$ was also observed in 8-m and 10-m depth by Kumar et al. (2016). Across all moorings, $\phi_1^{(SD)}(z/h)$ variability is elevated throughout the water column relative to other bands (Figure 6d, dashed lines), suggesting that a single vertical mode cannot represent the SD vertical structure at all moorings.

Because SD $\phi_1^{(SD)}(z/h)$ has the largest variability across moorings, the $\phi_1^{(SD)}(z/h)$ vertical structure is examined separately over all moorings relative to a linear Mode 1 baroclinic structure (i.e., normalized $\sin(\pi(z + h)/h)$) for depth-uniform $N^2$ (Figure 7). At some locations (e.g., northern and southern M1–M4, 13, 18, 19, and 20 in Figure 7), the SD $\phi_1^{(SD)}(z/h)$ vertical structure is similar to the linear baroclinic Mode 1 structure, indicating largely linear SD dynamics. In contrast, locations near Pt. Sal and Mussel Point with the subaqueous rocky outcrop (Figure 1c) have a strongly bottom intensified $\phi_1^{(SD)}(z/h)$ (e.g., M6–M9 in Figure 7) inconsistent with linear baroclinic Mode 1 structure, indicating nonlinear dynamics and suggesting near-bottom cold bores. Particular locations such as M12 in the bay south of Pt. Sal and M16 just north of Pt. Purisima have a quasi-barotropic vertical structure with a depth-uniform lower layer and weakly decaying upper layer (Figure 7). Although clearly not a linear baroclinic Mode 1, whether the SD processes inducing this vertical structure are more wavelike or advection is unclear.

### 3.5. Alongshore and Temporal Temperature Variability in the ST, DU, and SD Bands

The latitudinal dependence of the ST-temperature variability is examined at high alongshore resolution with a reconstructed near-surface $T_1^{(ST)}(y,t)$ from the mean $T(y,z)$ and the ST-first EOF. Consistent with previous observations (e.g., Cudaback et al., 2005; Melton et al., 2009), the predominant ST signals are largely northward propagating, SBC-origin warm water plumes associated with wind relaxations, with colder water conditions occurring in-between (Figure 8a). The first warm water plume (denoted as Plume 1, starting on Yearday 247) was strong, extending all the way north of Pt. Sal to M1 (Figure 8a) and occurring during a relatively long 10-day wind relaxation event (Yeardays 245–255; Figure 2b). The Melton et al. (2009) plume arrival time $t_{plume}$ (magenta dots in Figure 8a) has a quasi-linear latitude dependence. However, north of Pt. Purisima, and in particular north of Pt. Sal, warm water is seen to arrive well prior to $t_{plume}$. At the southernmost M20, Plume 1 induced an ≈6 °C temperature change, which slowly decayed northward as the plume propagated at roughly 22 km day$^{-1}$ from M20 to M1. The time ($t_{max}$) of Plume 1 maximum temperature $T_{max}$ also propagates northward, although not monotonically (yellow triangles, Figure 8a). South of Pt.
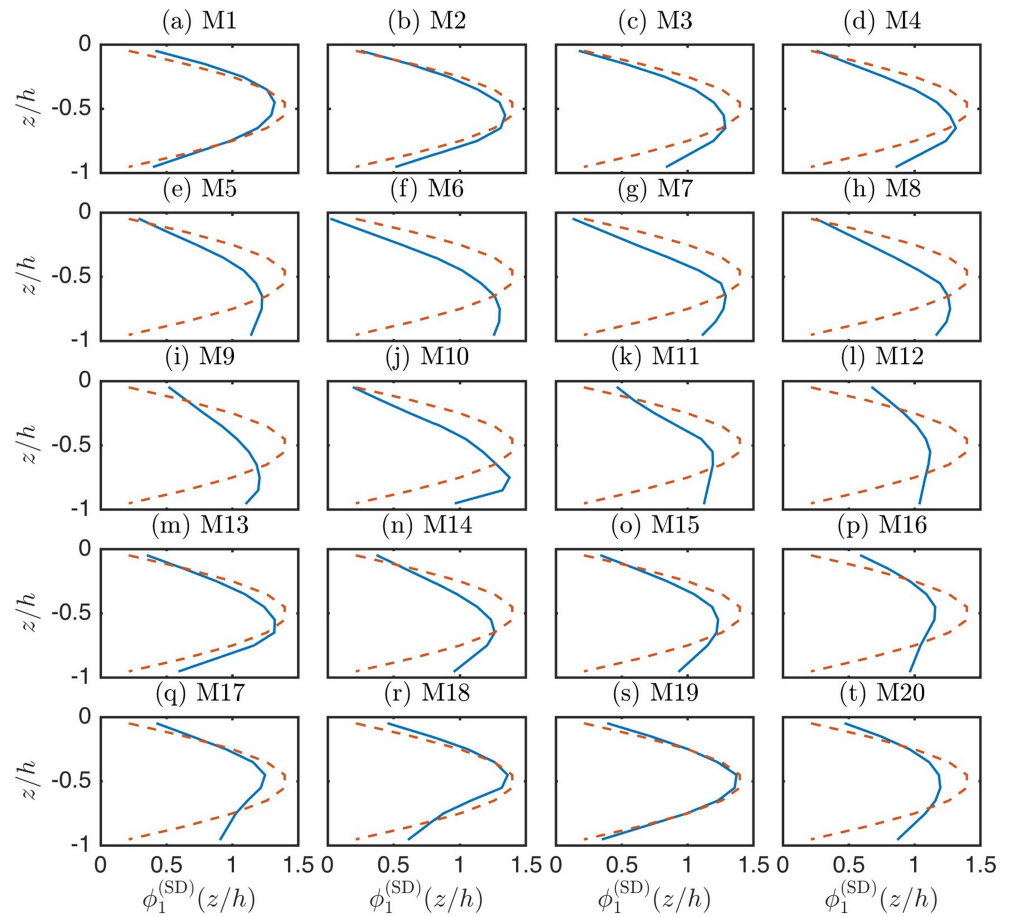
**Figure 7.** Semidiurnal band first EOF $\phi_1^{(SD)}(z/h)$ (blue lines) and normalized linear baroclinic Mode 1 structure, $\sin[\pi(z+h)/h]$ (orange dashed lines) as a function of normalized depth $z/h$ for the 20 moorings (Figure 1b) as indicated above each panel spanning a depth range of 9 to 16 m. The normalization is given in (1) and (3).

Purisima, the warm plume (>16 °C) lasted for ≈4 days. Plume duration increased north of Pt. Purisima (lasted for ≈5 days) and north of Pt. Sal (M1–M6) where the warm plume lasted for 10–15 days until Yearday 261. This increase in plume duration suggests interactions with the headlands. On Yeardays 256–258, a warm water event is present south of Pt. Sal with a weak southward-propagation sense (Figure 8a). Between Yeardays 262–264, another warm water feature with southward propagation is evident between M1 and M6 north of Pt. Sal (Figure 8a). Although these warm water features are not a traditional northward-propagating buoyant plume, they illustrate the complexity of nearshore temperature structure. On Yeardays 271 and 283, two weak warm water plumes (denoted as Plumes 2 and 3) propagated northward at ≈17 km day$^{-1}$ that only reached to M9 just south of Pt. Sal (magenta dots in Figure 8a). At M20, these plumes had a 2 °C and 3 °C temperature change and were associated with shorter 2- and 3-day wind relaxations (Figure 2b). Plumes 2 and 3 were similar and qualitatively different than the strong Plume 1, likely due to the differences in the duration of the wind relaxation (Melton et al., 2009). Because the ST EOF $\phi_1^{(ST)}(z/h)$ has a weak near-surface maximum (Figure 6b), plume events also increases the ST stratification, consistent with previous observations (e.g., Melton et al., 2009). Plume statistics are examined in detail in section 3.7.

Inner-shelf DU-band temperature variability is always present, and $A_1^{(DU)}(y, t)$ varies ±1 °C, with strongest variability in the entire region occurring north of Pt. Sal. The weakest $A_1^{(DU)}(y, t)$ variability is south Pt. Purisima (Figure 8b). Just south of Pt. Sal, the $A_1^{(DU)}(y, t)$ variability is also very weak. The DU-band variability is always present but is strongest from Yeardays 250–270 north of Pt. Purisima (Figure 8b). The $A_1^{(DU)}$
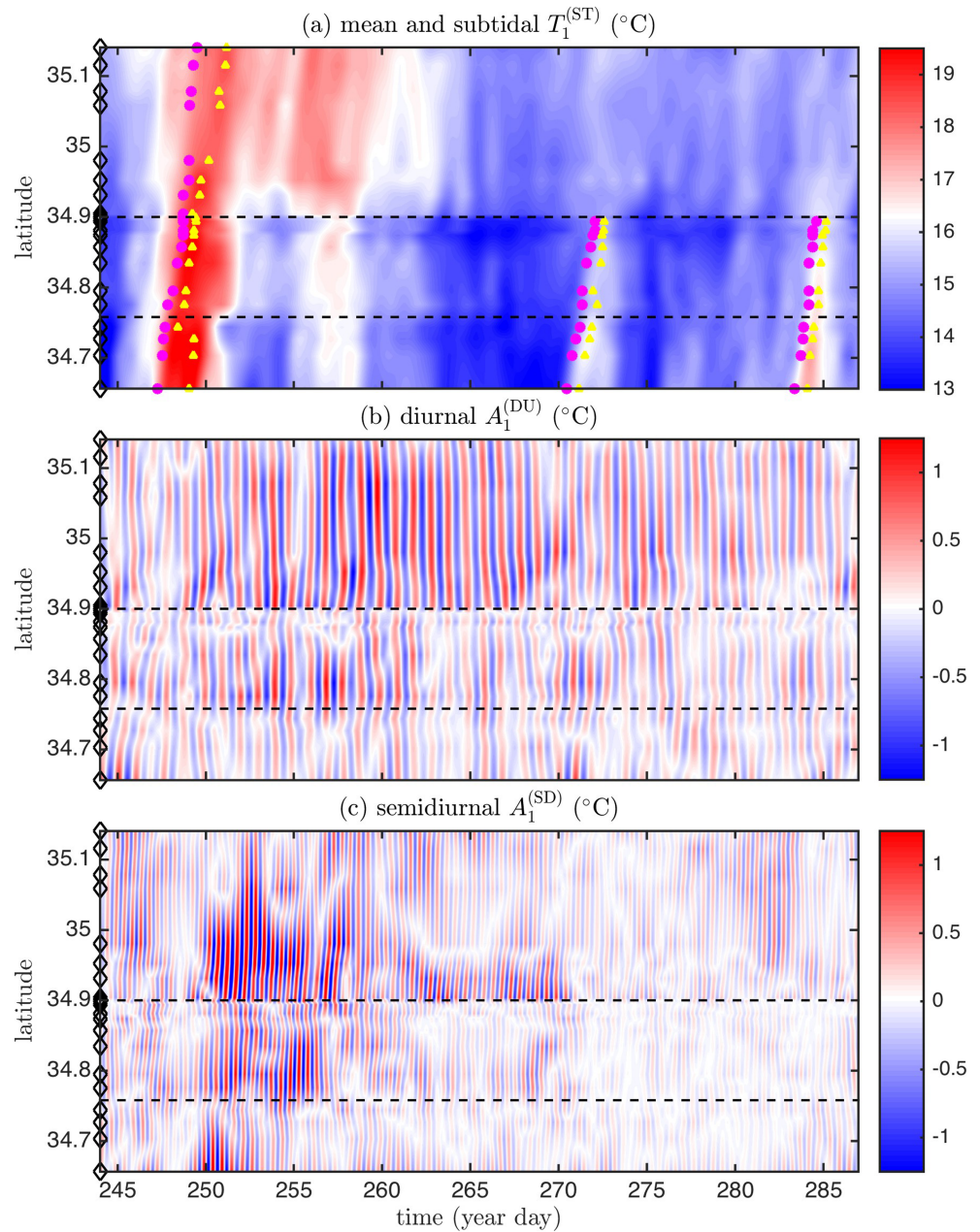
**Figure 8.** Hovmoller diagrams of (a) mean plus reconstructed first EOF subtidal near-surface temperature and first EOF amplitude (b) $A_1^{(DU)}$ and (c) $A_1^{(SD)}$ as a function of latitude and yearday. Horizontal dashed black lines indicate the locations of Pt. Sal and Pt. Purisima. The color scale represents temperature in degree Celsius. Diamonds on the ordinate represent mooring locations. In (a), magenta circles and yellow triangles indicate the warm plume arrival time ($t_{plume}$) and the time ($t_{max}$) of warm plume maximum temperature ($T_{max}$), respectively (see section 2.3), of the three warm plumes.

$(y, t)$ variability is not modulated by the ST changes in stratification. Correlations between the (Hilbert transform derived) envelope of $A_1^{(DU)}(y, t)$ and $A_1^{(ST)}(y, t)$ are not significant (at 95% confidence) at any location. This contrasts with Cudaback and McPhee-Shaw (2009) and Aristizabal et al. (2017) who suggested that the increased stratification of ST warm plumes increased the DU-$T$ signal.

In the SD band, $A_1^{(SD)}(y, t)$ varies $\pm 1.5$ °C (Figure 8d) with strongest variability between 34.9°N and 35.0°N in the region near and north of Pt. Sal. The largest SD variability occurs between Yeardays 250–258 (Figure 8d)

along the straight coasts north of Pt. Sal and Pt. Purisima (Figure 1b). The SD variability is less spatially coherent than the DU variability. Consistent with previous studies (Aristizabal et al., 2017), the ST-varying stratification associated with plume events modulates the SD variability (Figures 8a and 8c). As with the midwater column temperature spectra (Figure 5), the $A_1^{(SD)}(y, t)$ has broad SD peaks. At each mooring, applying a harmonic analysis (i.e., $T$ tide; Pawlowicz et al., 2002) reveals that >93% of the $A_1^{(SD)}(y, t)$ is incoherent with the M2, N2, and S2 barotropic tides.

### 3.6. Latitudinal Bulk Temperature and Stratification Statistics

The latitudinal variability and the influence of the Pt. Sal and Pt. Purisima headlands are evident with time-averaged statistics. Although most of the array is in 9-m depth, locations near the rocky Pt. Sal headland were in deeper depths from 10–16 m (Figure 9a). The time-averaged (over experiment duration) near-surface temperature $T_s$ varies from 14.7 °C to 15.9 °C, with a general warming trend from south to north with colder $T_s$ located just south of the two points, particularly at Pt. Sal (Figure 9b). The latitudinal variation in mean stratification $N^2$ is qualitatively similar to that of $T$ (Figures 9b and 9c) with $N^2$ generally largest to the north (near 35.1°N) and decreasing towards Pt. Sal (Figure 9c). Just south of Pt. Sal, $N^2$ weakens and subsequently increases toward Pt. Purisma, where it is relatively uniform from 35.85°N to 34.65°N (Figure 9c). The ST-band stratification variability (gray shading in Figure 9c) associated with relaxation and upwelling events is the largest north of Mussel Pt. at 25% of the mean and weaker south of Pt. Sal at about 12% of the mean. In the ST band, $\left(A_1^{(ST)}\right)^{2\frac{1}{2}}$ is relatively uniform in latitude, increasing gently to the south closer to the warm water source and with a sharp gradient just south of Pt. Sal (Figure 9d). In the DU band, $\left(A_1^{(DU)}\right)^{2\frac{1}{2}}$ is the largest north of Pt. Sal and is roughly constant from 35.07°N to Pt. Sal (Figure 9e). Just south of Pt. Sal, a sharp reduction of $\left(A_1^{(DU)}\right)^{2\frac{1}{2}}$ occurs, which gently increases southward towards Pt. Purisima. South of Pt. Purisima, $\left(A_1^{(DU)}\right)^{2\frac{1}{2}}$ is also reduced before increasing gently farther south. The 0.2–0.4 °C $\left(A_1^{(DU)}\right)^{2\frac{1}{2}}$ observed here during Fall 2017 (Figure 9e) is consistent with DU-$T$ variability observed just offshore in 50- to 100 m depth (Pidgeon & Winant, 2005), in 15-m depth south of Pt. Sal and Purisima (Cudaback & McPhee-Shaw, 2009), and near-bed DU-$T$ variability over multiple years (Aristizabal et al,. 2016). The spatial pattern of the dominant SD variability $\left(A_1^{(SD)}\right)^{2\frac{1}{2}}$ is similar to that for DU variability (Figure 9f), also highlighting the strong effects of the headlands.

### 3.7. ST Warm Plume Statistics

Here, the high alongshore mooring density is used to examine the alongshore variability of ST plume statistics (see section 2.3) for the three warm plumes identified in Figure 8a. Note, plume arrival time, maximum $T$, and time to maximum $T$ are differenced (denoted with symbol $\Delta$) relative to the southernmost mooring M20, yielding $\Delta t_{plume}$, $\Delta T_{max}$, and $\Delta t_{max}$. Plumes 2 and 3 were weak and were relatively consistent with a canonical largely shoreline-attached alongshore-propagating buoyant plume (e.g., Lentz & Helfrich, 2002; Melton et al., 2009; Washburn et al., 2011). Plumes 2 and 3 have quasi-constant propagation rates (at 19 and 15 km day$^{-1}$, respectively) that were consistent between $\Delta t_{plume}$ and $\Delta t_{max}$ (Figures 10a and 10d). Removing the Melton et al. (2009) criterion requiring plume arrival at location just south did not change $\Delta t_{plume}$. Note that Plume 3 propagation rate increases between Pt. Purisima and Pt. Sal (yellow, Figure 10 a). The Plumes 2 and 3 arrival temperature $T_{plume}$ is relatively constant (Figure 10b) at 15 °C (Plume 2) and 16 °C (Plume 3), suggesting a roughly latitude-independent plume arrival temperature. However, Plume 2 $T_{plume}$ is minimum at the southernmost M20 and increases by 0.5 °C near Pt. Sal. In contrast, Plume 3 $T_{plume}$ decreases northward with by 0.9 °C variation. Plumes 2 and 3 $\Delta T_{max}$ generally decays northward, but not smoothly nor even monotonically, with clear headland influence (Figure 10c). For example, the Plume 2 $\Delta T_{max}$ first increases 0.4 °C at M17–M19 before decreasing 0.6 °C at M16 north of Pt. Purisima and no clear tendency between Pt. Purisima and Pt. Sal (orange line, Figure 10c). In contrast, Plume 3 $\Delta T_{max}$ decreases 1.2 °C to Pt. Sal, with the strongest decreases south of Pt. Purisima and Pt. Sal (yellow line, Figure 10c). Plumes 2 and 3 are not observed north of Pt Sal. For Plume 2, this likely represents a
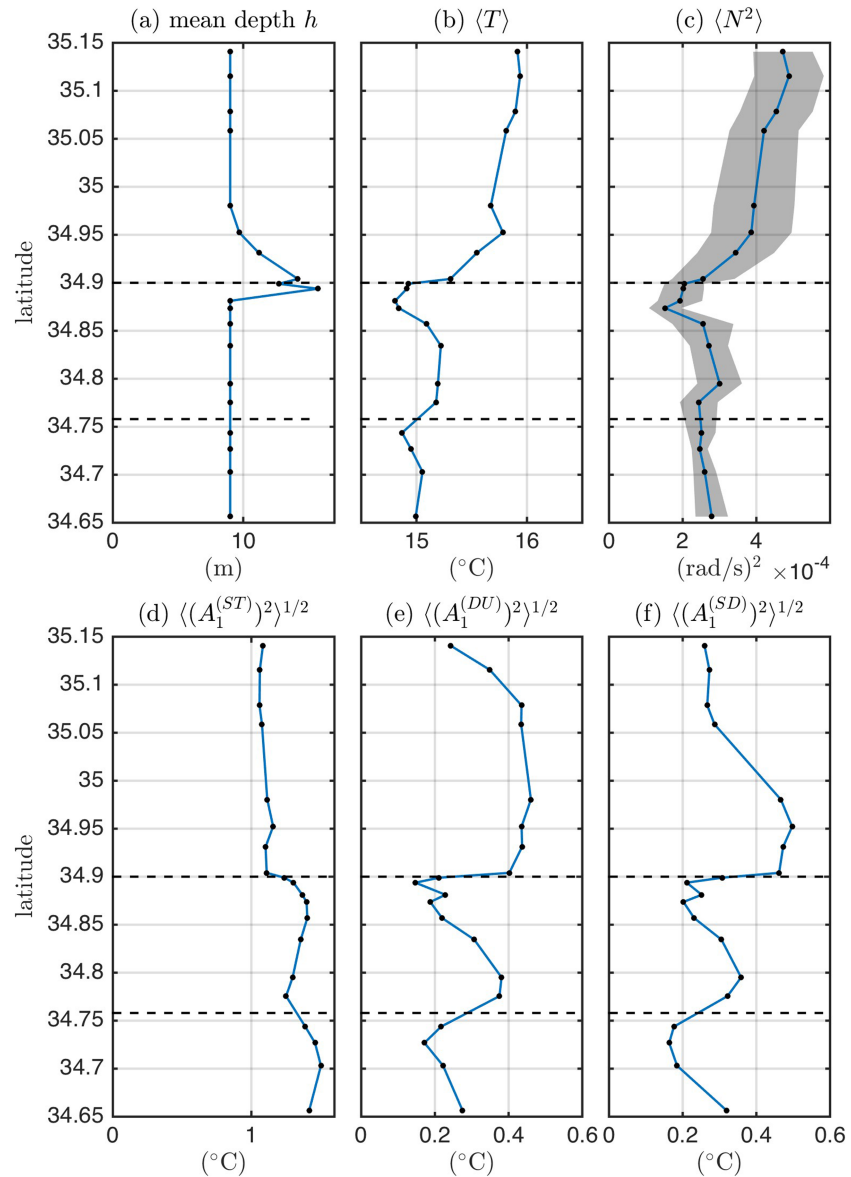
**Figure 9.** Mooring temperature statistics (blue curve and dots) versus latitude: (a) mean depth, (b) mean (time-averaged) temperature $T$ at near-surface location $z = -1.7$ m below mean tide level, (c) mean buoyancy frequency squared $N^2 \pm$ ST-band standard deviation (shading), (d) subtidal first EOF amplitude standard deviation $\left(A_1^{(ST)}\right)^{2^{1/2}}$, (e) diurnal first EOF amplitude standard deviation $\left(A_1^{(DU)}\right)^{2^{1/2}}$, (f) semidiurnal first EOF amplitude standard deviation $\left(A_1^{(SD)}\right)^{2^{1/2}}$. Horizontal dashed black lines indicate the locations of Pt. Sal and Purisima.

headland effect as the modeled relaxation winds are still active for 12–18 hr after Pt. Sal plume arrival (Figure 2b). Plume 3 has modeled relaxation winds end when $t_{\text{plume}}$ is at M19 south of Pt. Purisima. Plume 3 continued to propagate from M19 north to Pt. Sal (M9) with upwelling winds, also suggesting that Pt. Sal induced propagation to end. Thus, Plumes 2 and 3 are in many ways, but not completely, consistent with a buoyant plume on a uniform coastline. Plumes 2 and 3 headland effects are seen in the alongcoast variation in plume statistics.

Plume 1 has the largest temperature change and duration (Figure 8a) and is the least consistent with canonical buoyant plume on an alongshore uniform coast (Lentz & Helfrich, 2002). The Melton et al. (2009) Plume 1 arrival time $\Delta t_{\text{plume}}$ propagates roughly linear alongshore with some acceleration north of Pt. Sal (blue line in Figure 10a). The $T_{\text{plume}}$ is largely centered at 18 °C, is coldest at M20, and is as much as
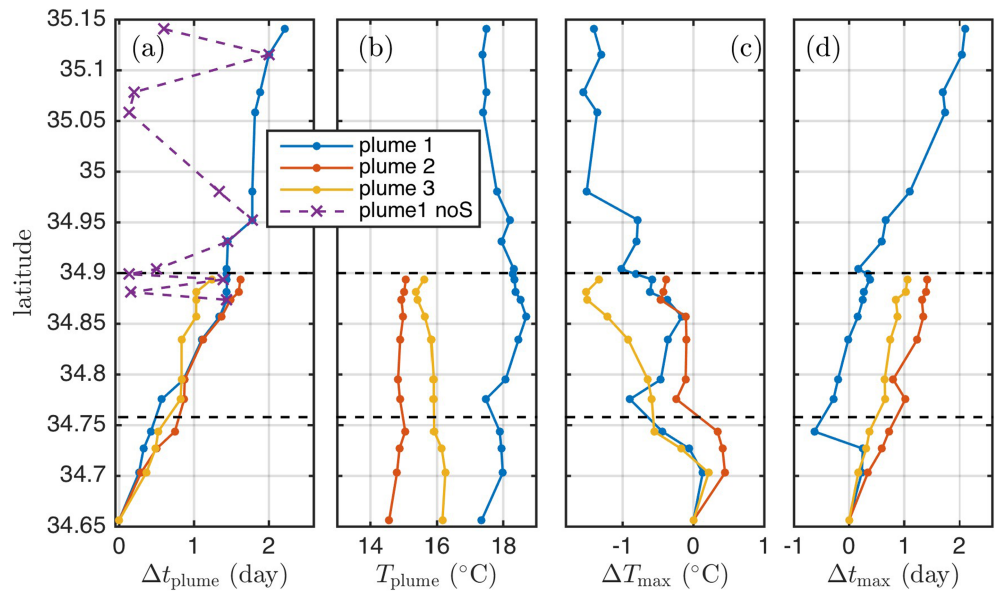
**Figure 10.** Subtidal warm plume statistics versus latitude for warm Plumes 1, 2, and 3 as indicated in the legend. (a) Warm plume arrival $\Delta t_{\text{plume}}$ (following Melton et al., 2009), (b) temperature at plume arrival $T_{\text{plume}}$, (c) maximum temperature $\Delta T_{\text{max}}$, and (d) arrival time of maximum temperature $\Delta t_{\text{max}}$. In panels (a, c, and d), statistics are differenced relative to the southernmost mooring M20 or 34.65°N (see section 2.3). The horizontal dashed lines represent the locations of Pt. Purisima and Pt. Sal. In panel (a), the purple symbols indicate Plume 1 arrival and temperature if the Melton et al. (2009) requirement of prior southern arrival is not included (denoted "noS" in the legend).

1.3 °C warmer at M13 (blue in Figure 10b). If the Melton et al. (2009) criteria of prior southward arrival were not applied for $\Delta t_{\text{plume}}$, locations near and north of Pt. Sal would have identified plume arrival earlier than those farther south (Figure 10a; compare blue line and purple associated with and without the criterion, respectively). Plume 1 warm water arrival prior to $t_{\text{plume}}$ is clearly seen in Figure 8a. Without the additional southward arrival criterion, plume arrival (purple in Figure 10a) near both Pt. Sal (M9) and at M4 occured at 3 hr after M20 arrival, equivalent to 2.1 and 3.5 m/s, far too fast to be alongshore advection. The Plume 1 $\Delta T_{\text{max}}$ evolution is also dramatic, decreasing 1 °C and increasing 1 °C between M20 and Pt. Sal (Figure 10c). North of Pt. Sal, $\Delta T_{max}$ is largely less than −1 °C but is not monotonic. This is counter to the near constant to decreasing $\Delta T_{\text{max}}$ expected for uniform coastline buoyant plume with infinite source. All of this indicates that the Plume 1 warm water pathway had an offshore component that was advected onshore between Pt. Purisima and Pt. Sal, as well as north of Pt. Sal.

### 3.8. Diurnal Band Analysis: Wind forcing and Alongshore Propagation

Previously, inner-shelf DU temperature variability in the Pt. Sal, Pt. Purisima, and SBC regions has been linked to DU wind forcing (e.g.,Aristizabal et al., 2016; Cudaback & McPhee-Shaw, 2009). Here, we examine whether the DU wind forcing is directly forcing the DU-$T$ variability. At each mooring, the envelope of the DU (easting and northing) winds and the envelope of the DU temperature $A_1^{(DU)}(y, t)$ is calculated with a Hilbert transform. The correlation between DU northing winds ($v$) and $T$ varies ±0.2 at all mooring locations (Figure 11, orange) and is not statistically significant at the 95% level (using a decorrelation time of 96 hr). For the DU easting winds ($u$), the correlation magnitude is larger at some locations at ±0.5 (Figure 11, blue) but only statistically significant for one mooring near Pt. Sal (filled blue symbol in Figure 11). However, this correlation is negative, indicating that strong DU-$T$ variability occurs during weak DU winds. Thus, we conclude that the DU-$T$ variability is not directly driven by the wind.

To further evaluate DU-$T$ variability, $A_1^{(DU)}(y, t)$ is plotted as a function of local time of day in hours versus yearday at moorings M1 and M7 (Figure 12), separated by about 20 km. At each mooring, the $A_1^{(DU)}(y, t)$ daily maximum is generally phase locked (with some variability) with average maximum occurring around 1700 and 2200 (local time) for M1 and M7, respectively (Figure 12). Thus, M1 and M7 have a DU-$T$ variability
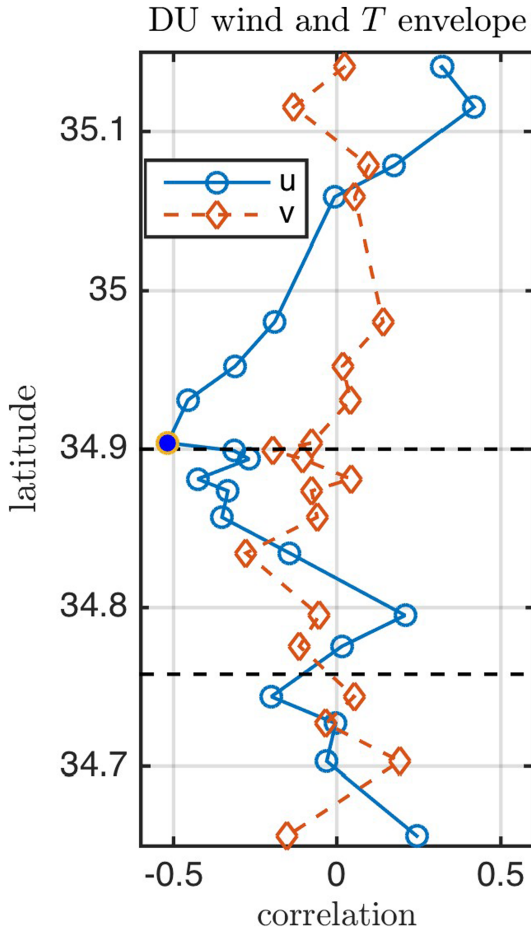
**Figure 11.** The correlation between the envelopes of diurnal EOF1 amplitude $A_1^{(DU)}(y, t)$ and COAMPS-modeled diurnal easting ($u$, blue circles) and northing ($v$, orange diamonds) winds. The horizontal dashed lines represent the locations of Pt. Sal and Pt. Purisima. The filled circle near Pt. Sal is significantly different from 0 at the 95% confidence level.

alongshore phasing with a 5-hr lag. For reference, the daily maximum DU winds consistently occur at 1600 (not shown).

To examine the alongshore coherent and propagating DU-$T$ variability, a Hilbert EOF (e.g., Horel, 1984) that resolves stationary and propagating covariability (e.g., Horel, 1984; Merrifield & Guza, 1990) is applied to $A_1^{(DU)}(y, t)$. For the DU band, a complex $A{*}_1^{(DU)}(y, t)$ time series is generated.

$$A{*}_1^{(DU)}(y, t) = A_1^{(DU)}(y, t) + i\widetilde{A}_1^{(DU)}(y, t), \tag{5}$$

where $\widetilde{A}_1^{(DU)}$ is the quadrature function (Hilbert transform) of $A_1^{(DU)}(y, t)$ and $i = \sqrt{-1}$. The $A{*}_1^{(DU)}(y, t)$ variability is decomposed into horizontal complex EOFs (CEOF), $H_n(y)$, such that

$$A_1{*}^{(DU)}(y, t) = \sum_{n=1}^{N} B_n(t) H_n^{(DU)}(y), \tag{6}$$

where the CEOFs $H_n^{(DU)}(y)$ are the eigenvectors of the Hermitian $A_1{*}^{(DU)}$ covariance matrix. The DU-first CEOF alongshore phase is estimated as

$$\theta_1^{(DU)}(y) = a\tan\left(\frac{\text{Im}\left[H_1^{(DU)}(y)\right]}{\text{Re}\left[H_1^{(DU)}(y)\right]}\right), \tag{7}$$

where Re and Im represent real and imaginary components. The alongshore DU magnitude is represented by $|H_1^{(DU)}(y)|$.

The first CEOF of alongshore DU temperature explains 67% of the latitudinal spatial variability. Consistent with large variance fraction explained, the first CEOF magnitude $|H_1^{(DU)}(y)|$ (Figure 13a) has a structure similar to $\left(A_1^{(DU)}\right)^{2\frac{1}{2}}$ (Figure 9d). The first CEOF phase $\theta_1^{(DU)}(y)$ reveals a coherent southerly propagation of 1.9 ms$^{-1}$ between 35.15°N and Pt. Sal (Figure 13b) with <5% propagating phase error (Merrifield & Guza, 1990), where the $|H_1^{(DU)}(y)|$ is largest (Figure 13a). Where $|H_1^{(DU)}(y)|$ is ele-

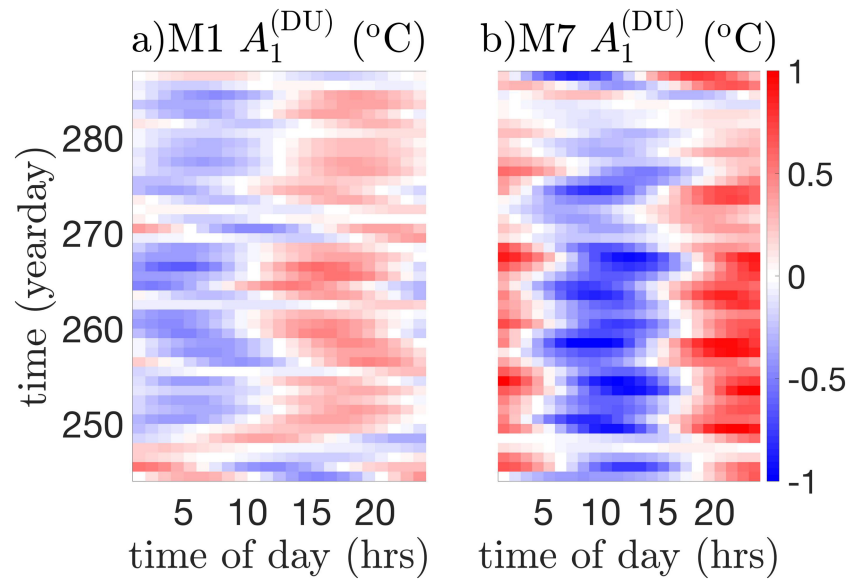vated between Pt. Sal and Pt. Purisima, the first CEOF phase $\theta_1^{(DU)}(y)$ also has a sense of coherent southerly propagation of 0.9 ms$^{-1}$, slower than north of Pt. Sal.

Even though the DU temperature $A_1^{(DU)}(y, t)$ is not related to the local DU wind envelope (Figure 11), it may be possible that the $A_1^{(DU)}(y, t)$ alongshore phase propagation is driven by an alongshore-propagating DU wind phase. Here, we test whether an alongshore-propagating modeled DU wind phase locally drives an alongshore-propagating DU-$T$ phase $\theta_1^{(DU)}(y)$ (Figure 13b). An alongshore CEOF decomposition was performed independently on the DU-band northing and easting winds (denoted with superscript "DW"). The first CEOF of easting and northing DU wind explains 93% and 68% of the DU wind variance, respectively, and the E and N magnitude $|H_1^{(DW)}(y)|$ varies by a factor of 2 over the study region (Figure 14a). However, the phase $\theta_1^{(DW)}(y)$ is relatively constant alongshore, indicating the DU winds are in phase alongshore (Figure 14b). Therefore, the observed DU temperature southward propagation also is not directly wind forced.

### 3.9. SD Band Depth-Integrated Energy, Decorrelation Length Scales, and Barotropic Tidal Coherence

For depth-uniform mean stratification $N^2$ (Figure 9c) and for kinetic and potential energy equipartition, the depth- and time-averaged SD energy $E^{(SD)}$, accurate to second order, is a function of the first EOF amplitude $A_1^{(SD)}$ and mean stratification $N^2$ as,

**Figure 12.** The DU EOF1 amplitude $A_1^{(DU)}(y, t)$ as a function of local time of day in hours and yearday for moorings (a) M1 and (b) M7.
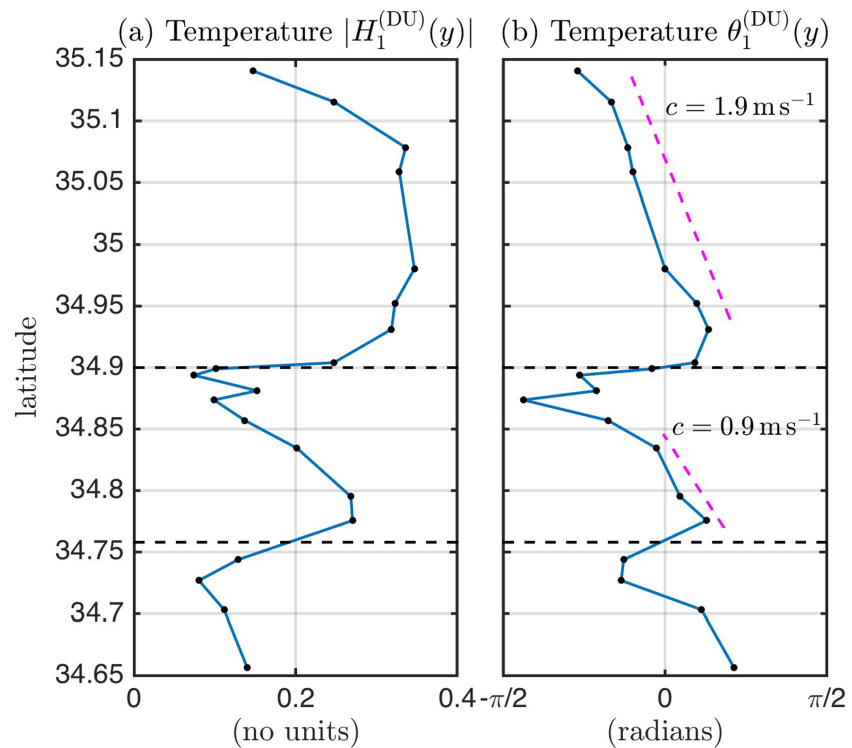


**Figure 13.** Alongshore diurnal temperature first Hilbert EOF versus latitude: (a) magnitude, $\left| H_1^{(DU)}(y) \right|$; and (b) phase, $\theta_1^{(DU)}(y)$. This first Hilbert EOF explains 67% of the spatial variability of the diurnal first EOF amplitude $A_1^{(DU)}(y, t)$ (2). Horizontal dashed black lines indicate the locations of Pt. Sal and Purisima. The magenta dashed lines indicate the inferred alongshore (latitude) propagation speeds north of Pt. Sal ($c = 1.9$ m/s) and between Pt. Sal and Pt. Purisima ($c = 0.9$ m/s).
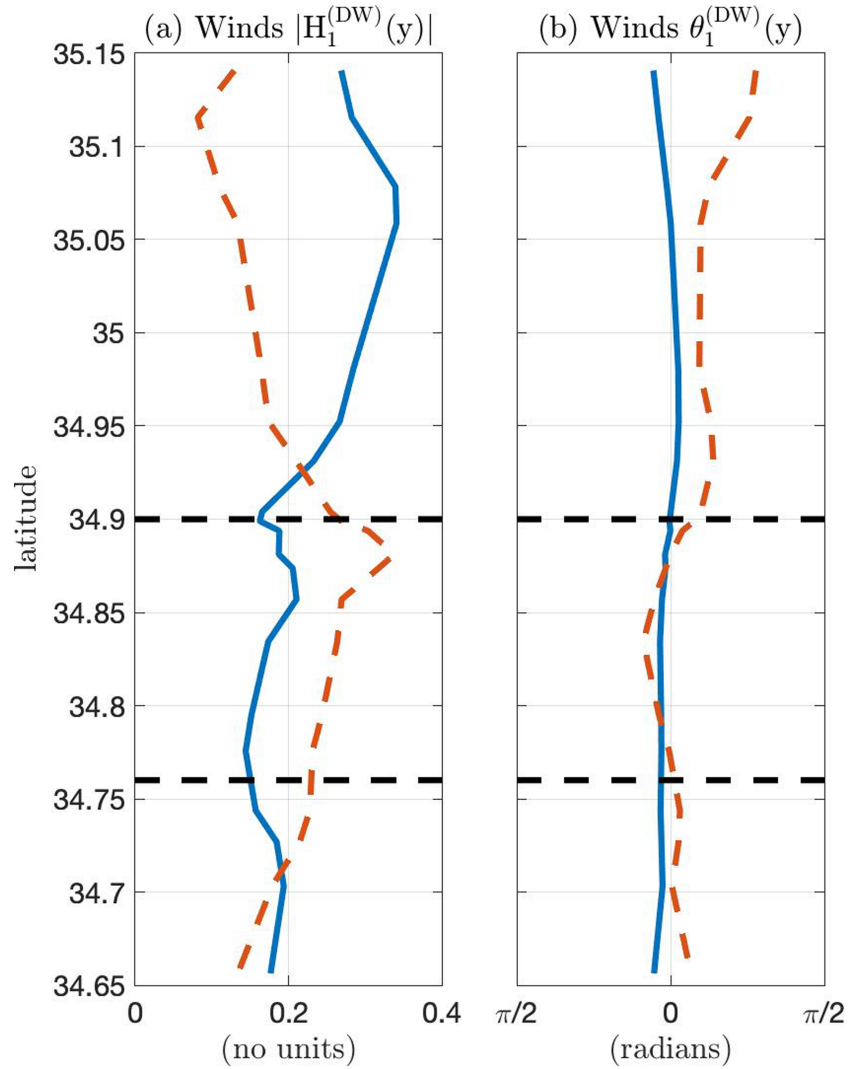
**Figure 14.** Alongshore first Hilbert EOF $H_1^{(DW)}(y)$ of the spatially interpolated COAMPS-modeled diurnal winds for easting ($u_e$, blue lines) and northing ($u_n$, orange lines) for (a) magnitude $|H_1^{(DW)}(y)|$ and (b) phasing, $\theta_1^{(DW)}(y)$, versus latitude. $H_1^{(DW)}(y)$ explains 93% of the spatial variability of the diurnal first amplitude. Horizontal dashed black lines indicate the locations of Pt. Sal and Purisima.

$$E^{(SD)} = \frac{g^2 \alpha^2 \left(A_1^{(SD)}\right)^2}{4\rho_o N^2}. \quad [J/m^2] \tag{8}$$

The expression for $E^{(SD)}$ is independent of $\phi_1^{(SD)}(z/h)$ because of the normalization (2). The depth-averaged energy (as opposed to depth integrated) is chosen to remove the effect of mooring depth variations (Figure 9a). Both standing and propagating energy $E^{(SD)}$ (e.g., Kumar et al., 2016; Lerczak et al., 2003) are included in (8). The latitudinal dependence of the SD-band energetics is examined with a normalized SD-band energy $\widetilde{E}^{(SD)}$, defined as

$$\widetilde{E}^{(SD)} = E^{(SD)}/\max\left(E^{(SD)}\right). \tag{9}$$

The SD depth-integrated energy $\widetilde{E}^{(SD)}$ varied strongly (factor 5×) alongshore in 9- to 16-m water depth, particularly south of Pt. Sal and Pt. Purisima (Figure 15), highlighting the strong effects of the headlands. The $\widetilde{E}^{(SD)}$ is weak (about 0.2) to the north, increases strongly south of 35 N toward a maximum $\widetilde{E}^{(SD)} = 1$ at Pt. Sal
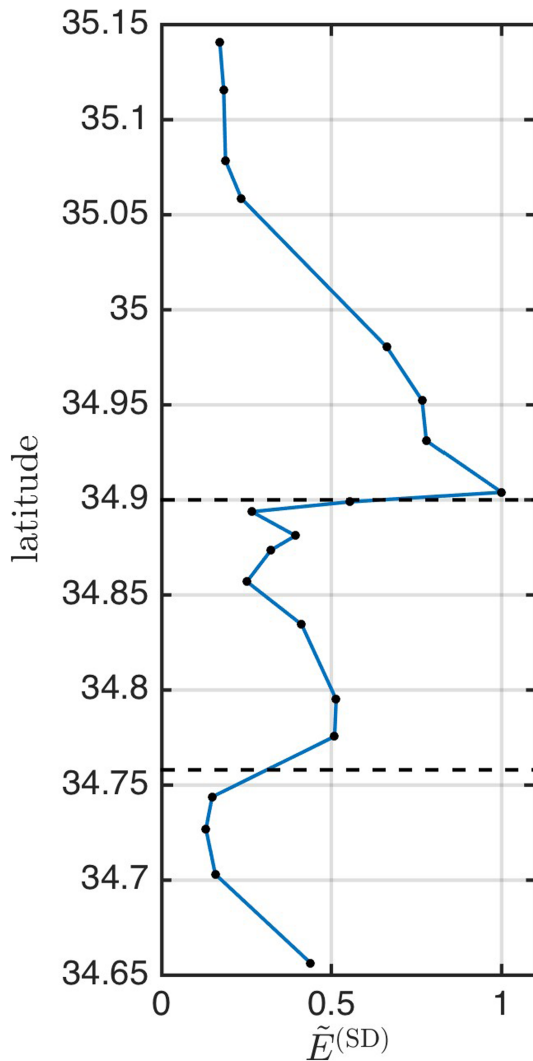
**Figure 15.** Normalized SD depth-averaged energy, $\widetilde{E}^{(SD)}$ (8 and 9) as a function of latitude. The locations of Pt. Sal and Purisima are indicated with the horizontal dashed lines.

(Figure 15), and sharply decreases by a factor of 4 just to the south of Pt. Sal. Just north of Pt. Purisima, a secondary $\widetilde{E}^{(SD)} = 0.5$ maximum occurs, which decays south of Pt. Purisima, although not as dramatically as at Pt. Sal (Figure 15). In contrast, the 50-m water depth incident SD-band energy flux varied weakly alongshore (spanning 7 km north and 3 km south of Pt. Sal) by a factor of 1.25× during June and July 2015 (Kumar et al., 2019). This suggests that the headlands bathymetry near refracted the incident SD energy onto the points, particularly Pt. Sal. Onshore of 50-m depth, SD-band energy is also likely dissipating (Colosi et al., 2018), reflecting (e.g., Kumar et al., 2016; Lerczak et al., 2003) or being transferred to higher frequencies (e.g., Holloway et al., 1999). The weak $\widetilde{E}^{(SD)}$ at M10 (in the bay south of Pt Sal, Figure 1c) is likely due, in part, to strong bathymetric refraction within the bay and also the shallower bathymetric slopes (relative to M8 at Pt. Sal) giving greater propagation distance for dissipation.

Any spatial coherence of the SD band $A_1^{(SD)}(y, t)$ (Figure 8c) is less clear than for ST or DU variability (Figures 8a and 8b). SD band $A_1^{(SD)}(y, t)$ alongshore spatial decorrelation scales are estimated from lagged cross-correlation analysis. Lagged $A_1^{(SD)}(y, t)$ cross-correlation functions, $r_{i,j}$, are estimated over all mooring pairs for 48-hr window, such that

$$\frac{r_{i,j}(\tau) = E\left[A_1^{(SD)}(y_i, t)\, A_1^{(SD)}(y_j, t + \tau)\right]}{E\left[A_1^{(SD)}(y_i, t)\, A_1^{(SD)}(y_j, t)\right],} \tag{10}$$

where $E$ is the expectation operator, $i$ and $j$ denote unique pair of moorings, $t$ is time, and $\tau$ is the temporal lag. The maximum $r_{i,j}(\tau)$ per mooring pair is referred to as $r_{max}^{(SD)}$ and is averaged in 3-km spatial bins. The $r_{max}^{(SD)}$ decays rapidly with alongshore instrument separation (Figure 16) with an $e$-folding decay scale of 7.5 km, indicating that $T_1^{(SD)}(y, t)$ decorrelates on relatively short alongshore spatial scales. Although the $A_1^{(SD)}(y, t)$ variance (and $\widetilde{E}^{(SD)}$) largely vary smoothly with latitude, except near Pt. Sal (Figure 9e), SD-$T$ variability is only coherent over short distances relative to the ST (Figure 8a) and DU (Figure 13) variability. These short (7.5 km) SD-band alongshore decorrelation length scales (Figure 16) are consistent with the spatially incoherent SD-band near-bed temperature variability between south of Pt. Sal and south of Pt. Purisima (Aristizabal et al., 2016).

At moorings M1–M20 (9- to 16-m water depth), the $A_1^{(SD)}(y, t)$ have broad spectra consistent with the M1 and M7 middepth temperature spectra (Figure 5). At all moorings, very little of the variability (<7%) is coherent with SD tidal frequencies (M2, N2, and S2). In contrast, in 50-m water depth offshore of Pt. Sal in Summer 2015, about half of the SD energy flux was coherent (i.e., at SD tidal frequencies M2, N2, and S2) and half incoherent in both observations and models (Kumar et al., 2019). This indicates that the variable stratification and Doppler shifting processes that induce SD baroclinic tidal incoherence are far larger in the 3–5 km between the 50-m and 10-m depth contour than in the approximately 100-km distance to the generation sites (Kumar et al., 2019).

## 4. Discussion

### 4.1. ST Warm Buoyant Plumes

ST poleward-propagating warm buoyant plumes, originating from the SBC, were previously studied in detail from north of Pt. Conception to south of Pt. Sal with three nearshore mooring locations on the south side of
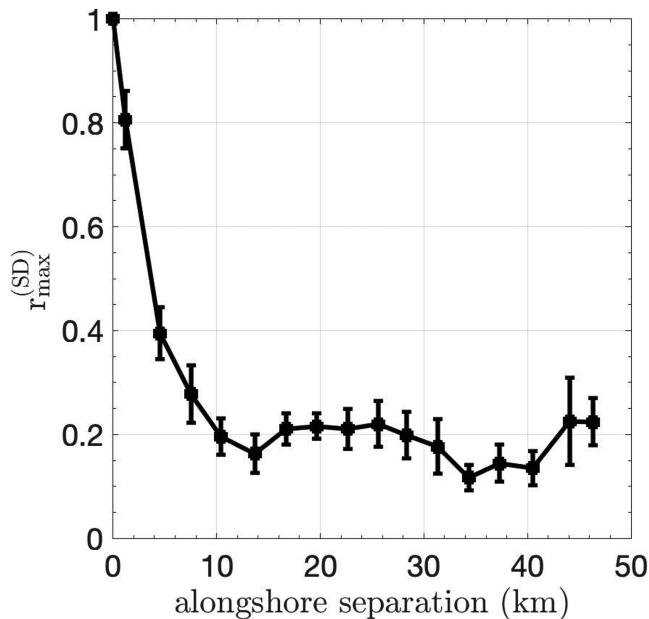
**Figure 16.** Maximum SD band $A_1^{(SD)}$ cross-correlation coefficient $r_{max}^{(SD)}$ (10) versus alongshore separation. The $r_{max}^{(SD)}$ is bin-averaged over 3 km, and mean (black squares) and 95% confidence interval (vertical lines) are shown.

the topographic points separated by 15–40 km (Cudaback et al., 2005; Melton et al., 2009 ; Washburn et al., 2011). The interpretation (Suanda et al., 2016; Washburn et al., 2011) drew on the theoretical model of a two-fluid gravity current on an alongshore-uniform sloping bathymetry (Lentz & Helfrich, 2002). Here, the high alongshore resolution array that extended north of Pt. Sal (Figure 1) allowed headland and offshore recirculation effects on three warm plumes to be observed, in contrast to the Lentz and Helfrich (2002) model. Plumes 2 and 3 are in many ways, but not completely, consistent with what would be expected for a warm buoyant plume for a coastline without headlands. Plumes 2 and 3 headland effects were seen in $\Delta T_{max}$, $T_{plume}$, and in propagation limited to Pt. Sal (Figure 10), even with wind relaxation conditions. For the strong Plume 1 that occurred during a long (10 days) wind relaxation, warm water arrived north of Pt. Sal within 3 hr of south of Pt. Purisima (Figure 10a), much too fast for a northward-flowing current and implying onshore advection of warm water due to other processes (Nidzieko & Largier, 2013). Thus, the Melton et al. (2009) prior southern arrival criteria bias to inferred northward propagation and give the appearance of consistency with the Lentz and Helfrich (2002) model. Furthermore, previously estimated $\Delta t_{plume}$ (Melton et al., 2009; Washburn et al., 2011) is aliased with the large mooring spacing. The headlands may induce offshore transport of warm plume water. For example, anticyclonic eddies that can develop between Pt. Arguello and Pt. Purisima as observed by Washburn et al. (2011). This eddy could deflect the warm SBC plume offshore, with potential for reconnection north of Pt. Sal. Another possible mechanism for warm water development north of Pt. Sal is the Pt. San Luis (Figure 1) upwelling shadow that tends to occur in late summer through early fall (Walter et al., 2018). Furthermore, clear Plume 1 headland effects are seen in $\Delta T_{max}$ and $\Delta t_{max}$ (Figures 10c and 10d and 8a). Thus, Plume 1 is largely inconsistent with the Lentz and Helfrich (2002) model north of Pt. Purisima, and further consideration of headland coastline effects on the propagation and mixing of buoyant thermal plumes is needed.

### 4.2. Diurnal Temperature Variability

The SMB DU vertical temperature structure in 50- to 100-m depth had a near-surface maximum, suggesting surface forcing (Pidgeon & Winant, 2005). In the SBC, the DU temperature first EOF had weak surface and bottom-enhanced structure (Cudaback & McPhee-Shaw, 2009). Aristizabal et al. (2016) observed that the DU winds and DU near-bed temperature were in phase in the SBC, concluding that DU temperature signal was directly DU wind forced and did not propagate alongshore. Cudaback and McPhee-Shaw (2009) stated that the DU wind variance forced DU temperature variance in the SBC but did not present statistics. Here, the first DU EOF (Figure 6c) had a mixed barotropic and linear baroclinic vertical structure, suggesting surface forcing is not the dominant process. The lack of an observed relationship between envelopes of the DU (easting and northing) winds and DU temperature $A_1^{(DU)}(y, t)$ (Figure 11) indicates that direct wind forcing did not drive the DU temperature variability in 9- to 16-m water depth along this stretch of coastline, counter to previous conclusions.

The DU temperature has a linear southward phase propagation of 1.9 m/s over a region of 18 km between SLO Bay and north of Pt. Sal (Figures 12 and 13b). Such southward alongcoast phase propagation for the subcritical DU frequencies has not been previously observed. The inferred phase speed is too rapid to be advection. A sense of southerly propagation also occurs between Pt. Sal and Pt. Purisima (Figure 13b). A barely significant DU temperature coherence between locations south of Pt. Sal and south of Pt. Purisima was noted by Cudaback and McPhee-Shaw (2009), consistent with the reduced Hilbert EOF amplitude south of the points (Figure 13). A southward-propagating inner-shelf DU-$T$ signal was inferred south of the San Diego Bay entrance (Grimes et al., 2019). These phase speeds may be larger than the actual propagation speeds if the propagation direction is not alongshore aligned. The uniform alongshore phase of the DU-modeled COAMPS winds (Figure 14b) indicates that the DU winds do not match DU-band $A_1^{(DU)}(y, t)$

southward phase propagation. This further demonstrates that DU temperature variability is not driven by the DU winds.

At this latitude, inviscid DU internal motions are evanescent as DU frequency $\omega_{\mathrm{DU}} < f$. Yet, when ST vorticity sufficiently reduces the local Coriolis parameter, DU internal waves can exist (e.g., Lerczak et al., 2001). However, the ubiquitous DU temperature variability during northward and southward flow periods (Figure 8b; Aristizabal et al., 2016; Pidgeon & Winant, 2005) suggests that this is not the mechanism allowing propagation here. In the SBC, the ST vorticity did not influence elevated DU temperature variability (Cudaback & McPhee-Shaw, 2009). An internal Kelvin or shelf mode (e.g., Mysak, 1980) could support frequencies less than $f$, but it would propagate northward. Furthermore, if this was a propagating internal wave, a strong baroclinic vertical structure would be expected, as opposed to the mixed barotropic and baroclinic vertical structure (Figure 6c).

One proposed mechanism for the observed alongshore-propagating DU-$T$ north of Pt. Sal is a forced DU-$T$ oscillation north of the array that propagates alongcoast as a baroclinic edge mode, where the presence of friction allows for propagation. Walter et al. (2017) found that the DU sea breeze transported surface warm water out of the SLO Bay (north of our array, Figure 1b) and transported near-bed colder water into the bay. When the DU sea breeze relaxed, warm water advected back into the bay as a buoyant plume. This headland-related DU forcing conceptually acts as a forced oscillator, which could set up baroclinic cross-shore standing modes (e.g., Llewellyn-Smith, 2004) that are typically alongcoast evanescent because the DU frequency $\omega_{\mathrm{DU}} < f$. The allowed northward-propagating Kelvin and shelf modes are not observed because SLO Bay source blocks northward propagation. However, friction is presumably significant for baroclinic motions in these shallow waters (e.g., Pringle & Brink, 1999). For a barotropic linear shallow-water $f$ plane with Rayleigh (linear) friction, the evanescent dispersion relationship is detuned and mixed decaying and southward-propagating solutions are allowed, that is, $\exp(-k_r y)$ $\exp[i(k_i y - R\omega_{\mathrm{DU}} t)])$ with $k_r > 0$ and $k_i < 0$ the real and imaginary parts of $k = (gh)^{-1/2} [(f^2 - \omega^2_{\mathrm{DU}}) - iR\omega_{\mathrm{DU}}]^{1/2}$, where $R$ is the Rayleigh drag coefficient. Although friction is often considered weak, when $\omega_{\mathrm{DU}}$ is near $f$, weak friction may become important. In principle, similar solutions should apply to $f$-plane frictional baroclinic modes on a slope extending the inviscid solutions of Llewellyn-Smith (2004). Solutions would depend critically on the cross-shore slope, stratification, and the Rayleigh drag coefficient as well as the local Coriolis parameter $f$ and DU frequency $\omega_{\mathrm{DU}}$. This analysis is to be presented elsewhere, and thus, this is only considered a proposed mechanism for the southward phase propagation.

### 4.3. SD Temperature Variability

The separation of SD temperature variability into vertical modes and alongshore structure elucidates how both the SD vertical structure (Figure 7) and the depth-integrated energy $\widetilde{E}^{(\mathrm{SD})}$ (Figure 15) vary alongshore. Previous SD-band temperature analyses over similar alongshore scales have focused on a single near-bed thermistor (e.g., Aristizabal et al., 2016), resulting in aliasing SD vertical structure into alongshore variability. For example, the ratio of near-bed $\phi_1^{(\mathrm{SD})}(z/h)$ between M14 and M1 is >2, even as their $\widetilde{E}^{(\mathrm{SD})}$ are similar. Using only near-bed thermistors would lead to the conclusion that M14 has much stronger SD variability than M1. Analysis in lower frequency bands (e.g., Tapia et al., 2014) does not have such aliasing problems as the vertical structure of low-frequency variability is much more depth uniform (Figure 6).

The alongshore-varying $\phi_1^{(\mathrm{SD})}(z/h)$ vertical structure (Figure 7) suggests that different locations support linear internal waves and nonlinear cold bores. SD-band internal waves are effective at transporting larvae and nutrients across the inner shelf (e.g., Lucas et al., 2011; Pineda, 1999), and variations in internal wave energy are linked to onshore larval recruitment (Pineda & Lopez, 2002). However, internal wave-induced transport likely depends on the vertical structure. Alongshore variations in SD temperature vertical structure (Figure 7) alone could reflect spatial variability of transport and potentially alongshore population variability. Locations with nonlinear internal waves would be expected to have larger energy $\widetilde{E}^{(\mathrm{SD})}$ than locations with a linear response. The relationship between the $\phi_1^{(\mathrm{SD})}(z/h)$ vertical structure and SD depth-averaged energy $\widetilde{E}^{(\mathrm{SD})}$ is examined here to better diagnose the processes driving the SD-$T$ variability. The misfit of $\phi_1^{(\mathrm{SD})}(z/h)$ from a linear Mode 1 baroclinic response $\sin[\pi (z+h)/h]$ (compare blue and orange dashed curves, Figure 7) is represented by mean square misfit $\epsilon^2$ defined as
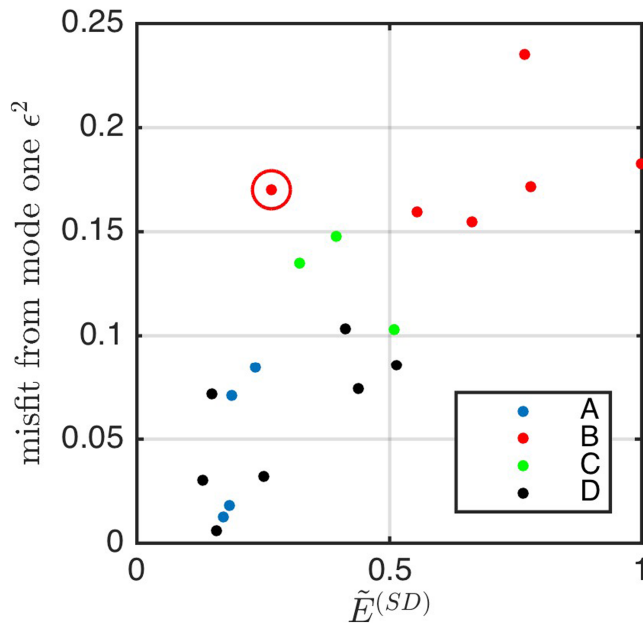
**Figure 17.** Normalized semidiurnal depth-averaged energy $\widetilde{E}^{(SD)}$ (8 and 9) versus misfit from baroclinic mode one $\epsilon^2$ (11). The squared correlation is $r^2 = 0.61$. Color represents heuristic groupings-based (A, B, C, and D) geography (Figure 1b) and on $\phi_1^{(SD)}(z/h)$ vertical structure (Figure 6) as discussed in section 4.3. Red-circled red dot represents results from M10.

$$\epsilon^2 = \int_{-1}^{0} \left( \phi_1^{(SD)}\left(\frac{z}{h}\right) - sin[\pi\,(z/h + 1)] \right)^2 d(z/h)\,, \qquad (11)$$

where $\epsilon^2 = 0$ is a linear Mode 1 response.

The misfit $\epsilon^2$ varies from 0.01 to 0.24, indicating near-exact to strong deviation from linear baroclinic response (Figure 17). The misfit $\epsilon^2$ and normalized SD energy $\widetilde{E}^{(SD)}$ are linearly related ($r^2 = 0.61$) with stronger energy related to larger misfit (Figure 17), consistent with linear baroclinic structure for weak SD internal tide and nonlinear bottom-intensified structure with stronger SD internal tides. The SD misfit and energy are heuristically grouped by geography and $\phi_1^{(SD)}(z/h)$ (colors in Figure 17). The generally largest $\widetilde{E}^{(SD)}$ and largest $\epsilon^2$ are clustered into a group, denoted as B (red in Figure 17), consisting of M5 to M10, all locations relatively close to Mussel Pt. and Pt. Sal, indicating that a regional internal wave hotspot. In contrast, the generally smallest $\widetilde{E}^{(SD)}$ and $\epsilon^2$ are associated with the locations near SLO Bay (M1–M4, Group A) or moorings near and south of Pt. Purisima (M13–M15 and M16–M20, Group D) consistent with weaker and more linear SD internal waves. Intermediate $\widetilde{E}^{(SD)}$ and $\epsilon^2$ located between Pt. Sal and Pt. Purisima (M11, M12, and M16; Group C) have quasi-barotropic $\phi_1^{(SD)}(z/h)$ induced by either am SD wave or advective process. This A–D grouping is heuristic, particularly for Groups C and D south of Pt. Sal. For example, M15 and M17 (Figure 7) could be in Group C and not Group D. Nevertheless, the relationship between $\widetilde{E}^{(SD)}$ and $\epsilon^2$ is robust and independent of this grouping.

Mooring M10 is located in the bay southeast of Pt. Sal (Figure 1c) and is an outlier in the linear relationship between $\widetilde{E}^{(SD)}$ and $\epsilon^2$ (red open circle of Group B, Figure 17). M10 has relatively large $\epsilon^2 = 0.17$, consistent with other moorings of its geographical grouping B but weak $\widetilde{E}^{(SD)} = 0.27$, relative to other Group B moorings (red, Figure 17). Mooring M10 is less than 2 km separated from the M8 just west of Pt. Sal (see Figure 1 c), which has the strongest $\widetilde{E}^{(SD)}=1$. M10 is the most sheltered mooring location and yet has vertical structure consistent with a nonlinear cold bore (Figure 7j). Offshore of M10 is also more shallowly sloped than at nearby locations (e.g., M8, M9, and M11; Figure 1c). The SD internal waves incident to Pt. Sal are strongly nonlinear (Colosi et al., 2018). The M10 deviation in the $\widetilde{E}^{(SD)}$ and $\epsilon^2$ relationship suggests that the cross-shelf nonlinear transformation of the SD-band internal waves into M10 is fundamentally different than at other locations.

## 5. Summary

The coastal region of the SMB has regions of relatively straight shorelines interrupted by coastal headlands such as Pt. Sal and Pt. Purisima. Twenty moorings with a high vertical density of thermistors were deployed in 9- to 16-m water depths along 50 km of this coastline to study the temporal, vertical, and alongshore inner-shelf temperature ($T$) variability. Temperature spectra had peaks with significant variability in the ST, DU, and SD frequency bands. At each mooring and in each frequency band, the vertical $T$ structure first EOF $\phi_1(z/h)$ describes a high fraction of variance. The ST vertical structure $\phi_1^{(ST)}(z/h)$ was quasi depth-uniform with weak linear vertical structure at all moorings. Wind relaxation induced three ST-band poleward-propagating warm plumes. The two weaker plumes were relatively consistent with alongshore uniform buoyant plume model, although headland effects were observed. The strongest plume had strong headland effects and offshore warm water advecting onshore, inconsistent with buoyant plume model. Previous plume arrival time criteria are biased to northward propagation, and the high alongcoast resolution prevented aliasing of plume statistics.

The DU-$T$ vertical structure $\phi_1^{(DU)}(z/h)$ was a mix of barotropic and linear baroclinic structure, without a surface extrema, indicating that surface forcing is not the dominant process. Inner-shelf DU-band temperature

variability with magnitude of 0.2–0.4 °C was always evident and was the largest north of Pt. Sal with sharp reductions south of Pt. Sal and Pt. Purisima. The time envelope of DU variability was not modulated by the ST stratification changes nor was it linked to the envelope of modeled DU winds, in contrast to previous studies. The alongshore first CEOF of DU temperature explains 67% of the latitudinal variability. The DU first CEOF has an alongshore linear phase variation north of Pt. Sal, suggesting a 1.9-m/s southerly propagation, even though DU frequency is subcritical at this latitude. The modeled DU winds had nearly uniform alongshore phase. This indicates that the DU winds do not directly generate this DU-$T$ southward phase propagation. The presence of friction allowing mixed decaying and propagating solutions is a proposed mechanism for the observed DU propagation.

In contrast to the DU and ST bands, the SD-$T$ vertical structure $\phi_1^{(SD)}(z/h)$ varies alongshore, suggesting at different locations linear internal waves and nonlinear cold bores. Inner-shelf SD-band temperature variability is modulated by the ST-band stratification, consistent with previous results. The SD depth-averaged energy varied strongly (factor 5×) alongshore particularly near the headlands, with locations near Mussel Pt. and Pt. Sal regional internal wave hotspots. SD-$T$ variability was incoherent with barotropic tides and decorrelates alongshore in 7.5 km, contrasting with SD-$T$ variability a few kilometers offshore. Enhanced and weaker SD depth-averaged energy was linked to nonlinear and linear baroclinic vertical structures, respectively, which are headland influenced. These alongshore variations in SD variability and vertical structure are likely important to material transport.

# References

Aristizabal, M. F., Fewings, M. R., & Washburn, L. (2016). Contrasting spatial patterns in the diurnal and semidiurnal temperature variability in the Santa Barbara Channel, California. *Journal of Geophysical Research: Oceans*, *121*, 427–440. https://doi.org/10.1002/2015JC011239

Aristizabal, M. F., Fewings, M. R., & Washburn, L. (2017). Effects of the relaxation of upwelling favorable winds on the diurnal and semidiurnal water temperature fluctuations in the Santa Barbara Channel, California. *Journal of Geophysical Research: Oceans*, *122*, 7958–7977. https://doi.org/10.1002/2017JC013199

Austin, J. A. (1999). The role of the alongshore wind stress in the heat budget of the North Carolina inner shelf. *Journal of Geophysical Research*, *104*, 18,187–18,203. https://doi.org/10.1029/1998JC900122

Boehm, A. B., Lluch-Cota, D. B., Davis, K. A., Winant, C. D., & Monismith, S. G. (2004). Covariation of coastal water temperature and microbial pollution at interannual to tidal periods. *Geophysical Research Letters*, *31*, L06309. https://doi.org/10.1029/2003GL019122

Bonicelli, J., Moffat, C., Navarrete, S. A., Largier, J. L., & Tapia, F. J. (2014). Spatial differences in thermal structure and variability within asmall bay: Interplay of diurnal winds and tides. *Continental Shelf Research*, *88*, 72–80. https://doi.org/10.1016/j.csr.2014.07.009

Colosi, J. A., Kumar, N., Suanda, S. H., Freismuth, T. M., & MacMahan, J. H. (2018). Statistics of internal tide bores and internal solitary waves observed on the inner continental shelf off Point Sal, California. *Journal of Physical Oceanography*, *48*(1), 123–143. https://doi.org/10.1175/JPO-D-17-0045.1

Cudaback, C. N., & McPhee-Shaw, E. (2009). Diurnal-period internal waves near Point Conception, California, Estuarine. *Coastal and Shelf Science*, *83*(3), 349–359. https://doi.org/10.1016/j.ecss.2008.12.018

Cudaback, C. N., Washburn, L., & Dever, E. (2005). Subtidal inner-shelf circulation near Point Conception, California. *Journal of Geophysical Research*, *110*, C10007. https://doi.org/10.1029/2004JC002608

Fewings, M. R., Washburn, L., & Ohlmann, J. C. (2015). Coastal water circulation patterns around the northern Channel Islands and Point Conception, California. *Progress in Oceanography*, *138*, 283–304. https://doi.org/10.1016/j.pocean.2015.10.001.16

Fewings, M. R., & Lentz, S. J. (2011). Summertime cooling of the shallow continental shelf. *Journal of Geophysical Research*, *116*, C07015. https://doi.org/10.1029/2010JC006744

Friedrichs, C. (1995). Stability shear stress and equilibrium cross-sectional geometry of sheltered tidal channels. *Journal of Coastal Research*, *11*, 1062–1074.

Godin, G., & Martínez, A. (1994). Numerical experiments to investigate the effects of quadratic friction on the propagation of tides in a channel. *Continental Shelf Research*, *14*(7-8), 723–748. https://doi.org/10.1016/0278-4343(94)90070-1

Grimes, D. J., Feddersen, F., Giddings, S. N., & Pawlak, E. A. (2019). Cross-shore deformation of a surfzone-released dye plume by an internal tide on the inner-shelf. *Journal of Physical Oceanography*, *50*(1), 35–54. https://doi.org/10.1175/JPO-D-19-0046.1

Hally-Rosendahl, K., Feddersen, F., & Guza, R. T. (2014). Cross-shore tracer exchange between the surfzone and inner-shelf. *Journal of Geophysical Research: Oceans*, *119*, 4367–4388. https://doi.org/10.1002/2013JC009722

Herdman, L. M. M., Hench, J. L., & Monismith, S. G. (2015). Heat balances and thermally driven lagoon-ocean exchanges on a tropical coral reef system (Moorea, French Polynesia). *Journal of Geophysical Research: Oceans*, *120*, 1233–1252. https://doi.org/10.1002/2014JC010145

Hodur, R. M. (1997). The Naval Research Laboratory's Coupled Ocean/Atmosphere Mesoscale Prediction System (COAMPS). *Monthly Weather Review*, *125*, 1414–1430. https://doi.org/10.1175/1520-0493(1997)125<1414:TNRLSC>2.0.CO;2

Holloway, P. E., Pelinovsky, E., & Talipova, T. (1999). A generalized Korteweg-de Vries model of internal tide transformation in the coastal zone. *Journal of Geophysical Research*, *104*(C8), 18,333–18,350. https://doi.org/10.1029/1999JC900144

Horel, J. D. (1984). Complex principal component analysis: Theory and examples. *Journal of Climate and Applied Meteorology*, *23*(12), 1660–1673. https://doi.org/10.1175/1520-0450(1984)023<1660:CPCATA>2.0.CO;2

Kaplan, D. M., Largier, J. L., Navarrete, S., Guinez, R., & Castilla, J. C. (2003). Large diurnal temperature fluctuations in the nearshore water column. *Estuarine, Coastal and Shelf Science*, *57*(3), 385–398. https://doi.org/10.1016/S0272-7714(02)00363-3

Kumar, N., Feddersen, F., Suanda, S., McWilliams, J. C., & Uchiyama, Y. (2016). Mid- to inner-shelf coupled ROMS-SWAN model-data comparison of currents and temperature: Diurnal and semidiurnal variability. *Journal of Physical Oceanography*, *46*(3), 841–862. https://doi.org/10.1175/JPO-D-15-0103.1

Kumar, N., Suanda, S. H., Colosi, J. A., Haas, K., di Lorenzo, E., Miller, A. J., & Edwards, C. A. (2019). coastal semidiurnal internal tidal incoherence in the Santa Maria Basin, California: Observations and model simulations. *Journal of Geophysical Research: Oceans*, *124*, 5158, 2018JC014891–5179. https://doi.org/10.1029/2018JC014891

Lentz, S. J., & Helfrich, K. R. (2002). Buoyant gravity currents along a sloping bottom in a rotating fluid. *Journal of Fluid Mechanics*, *464*, 251–278. https://doi.org/10.1017/S0022112002008868

Lerczak, J., Barth, J., Celona, S., Chickadel, C., Colosi, J., Feddersen, F., et al. (2019). Untangling a web of interactions where surf meets coastal ocean. *Eos*, *100*. https://doi.org/10.1029/2019EO122141

Lerczak, J. A., Hendershott, M. C., & Winant, C. D. (2001). Observations and modeling of coastal internal waves driven by a diurnal sea breeze. *Journal of Geophysical Research*, *106*(C9), 19,715–19,729. https://doi.org/10.1029/2001JC000811

Lerczak, J. A., Winant, C. D., & Hendershott, M. C. (2003). Observations of the semidiurnal internal tide on the southern California slope and shelf. *Journal of Geophysical Research*, *108*(C3), 3068. https://doi.org/10.1029/2001JC001128

Llewellyn-Smith, S. G. (2004). Stratified rotating edge waves. *Journal of Fluid Mechanics*, *498*, 161–170. https://doi.org/10.1017/S002211200300702X

Lucas, A. J., Franks, P. J. S., & Dupont, C. L. (2011). Horizontal internal-tide fluxes support elevated phytoplankton productivity over the inner continental shelf. *Limnology and Oceanography: Fluids and Environments*, *1*, 56–74. https://doi.org/10.1215/21573698-1258185

Lucas, A. J., Pitcher, G. C., Probyn, T. A., & Kudela, R. M. (2014). The influence of diurnal winds on phytoplankton dynamics in a coastal upwelling system off southwestern Africa. *Deep-Sea Research Part I-Topical Studies in Oceanography.*, *101*, 50–62. https://doi.org/10.1016/j.dsr2.2013.01.016

McPhee-Shaw, E. E., Siegel, D. A., Washburn, L., Brzezinski, M. A., Jones, J. L., Leydecker, A., & Melack, J. (2007). Mechanisms for nutrient delivery to the inner shelf: Observations from the Santa Barbara Channel. *Limnology and Oceanography*, *52*(5), 1748–1766. https://doi.org/10.4319/lo.2007.52.5.1748

McSweeney, J. M., Lerczak, J. A., Barth, J. A., Bechere, J., Colosi, J. A., MacKinnon, J. A., et al. (2019). Observations of shoaling nonlinear internal bores across the central California inner shelf. *Journal of Physical Oceanography*, *50*(1), 111–132. https://doi.org/10.1175/JPO-D-19-0125.1

Melton, C., Washburn, L., & Gotschalk, C. (2009). Wind relaxations and poleward flow events in a coastal upwelling system on the central California coast. *Journal of Geophysical Research*, *114*, C11016. https://doi.org/10.1029/2009JC005397

Merrifield, M., & Guza, R. (1990). Detecting propagating signals with complex empirical orthogonal functions: A cautionary note. *Journal of Physical Oceanography*, *20*(10), 1628–1633. https://doi.org/10.1175/1520-0485(1990)020<1628:DPSWCE>2.0.CO;2

Molina, L., Pawlak, G., Wells, J. R., Monismith, S. G., & Merrifield, M. A. (2014). Diurnal cross-shore thermal exchange on a tropical fore reef. *Journal of Geophysical Research: Oceans*, *119*, 6101–6120. https://doi.org/10.1002/2013JC009621

Mysak, L. A. (1980). Topographically trapped waves. *Annual Review of Fluid Mechanics*, *12*, 45–76. https://doi.org/10.1146/annurev.fl.12.010180.000401

Nam, S., & Send, U. (2013). Resonant diurnal oscillations and mean alongshore flows driven by sea/land breeze forcing in the coastal Southern California Bight. *Journal of Physical Oceanography*, *43*(3), 616–630. https://doi.org/10.1175/JPO-D-11-0148.1

Nidzieko, N. J. (2010). Tidal asymmetry in estuaries with mixed semidiurnal/diurnal tides. *Journal of Geophysical Research: Oceans*, *115*, C08006. https://doi.org/10.1029/2009JC005864

Nidzieko, N. J., & Largier, J. L. (2013). Inner shelf intrusions of offshore water in an upwelling system affect coastal connectivity. *Geophysical Research Letters*, *40*, 5423–5428. https://doi.org/10.1002/2013GL056756

O'Connor, M. I., Bruno, J. F., Gaines, S. D., Halpern, B. S., Lester, S. E., Kinlan, B. P., & Weiss, J. M. (2007). Temperature control of larval dispersal and the implications for marine ecology, evolution, and conservation. *Proceedings of the National Academy of Sciences of the United States of America*, *104*, 1266–1271. https://doi.org/10.1073/pnas.0603422104

Ohashi, K., & Wang, D. P. (2004). Circulation in the Santa Maria Basin, California, during 1998. *Journal of Geophysical Research*, *109*, C11012. https://doi.org/10.1029/2004JC002362

Pawlowicz, R., Beardsley, B., & Lentz, S. (2002). Classical tidal harmonic analysis including error estimates in MATLAB using T_TIDE. *Computers & Geosciences*, *28*(8), 929–937. https://doi.org/10.1016/S0098-3004(02)00013-4

Pidgeon, E. J., & Winant, C. D. (2005). Diurnal variability in currents and temperature on the continental shelf between central and southern California. *Journal of Geophysical Research*, *110*, C03024. https://doi.org/10.1029/2004JC002321

Pineda, J. (1999). Circulation and larval distribution in internal tidal bore warm fronts. *Limnology and Oceanography*, *44*(6), 1400–1414. https://doi.org/10.4319/lo.1999.44.6.1400

Pineda, J., & Lopez, M. (2002). Temperature, stratification and barnacle larval settlement in two Californian sites. *Continental Shelf Research*, *22*, 1183–1198. https://doi.org/10.1016/S0278-4343(01)00098-X

Preisendorfer, R. U. (1988). *Principal component analysis in meteorology and oceanography*, (Vol. 17). Oxford, United Kingdom: Elsevier Science & Technology.

Pringle, J. M., & Brink, K. H. (1999). High-frequency internal waves on a sloping shelf. *Journal of Geophysical Research*, *104*(C3), 5283–5299. https://doi.org/10.1029/1998JC900054

Sinnett, G., & Feddersen, F. (2019). The nearshore heat budget: Effects of stratification and surfzone dynamics. *Journal of Geophysical Research: Oceans*, *124*, 8219–8240. https://doi.org/10.1029/2019JC015494

Suanda, S. H., Barth, J. A., & Woodson, C. B. (2011). Diurnal heat balance for the northern Monterey Bay inner shelf. *Journal of Geophysical Research*, *116*, C09030. https://doi.org/10.1029/2010JC006894

Suanda, S. H., Kumar, N., Miller, A. J., Lorenzo, E. D., Haas, K., Cai, D., et al. (2016). Wind relaxation and a coastal buoyant plume north of Pt. Conception, CA: Observations, simulations, and scalings. *Journal of Geophysical Research: Oceans*, *121*, 7455–7475. https://doi.org/10.1002/2016JC011919

Tapia, F., Largier, J. L., Castillo, M., Wieters, E., & Navarrete, S. A. (2014). Latitudinal discontinuity in thermal conditions along the nearshore of central northern Chile. *PLOS ONE*, *9*, 1–11. https://doi.org/10.1371/journal.pone.0110841

Walter, R. K., Armenta, K. J., Shearer, B., Robbins, I., & Steinbeck, J. (2018). Coastal upwelling seasonality and variability of temperature and chlorophyll in a small coastal embayment. *Continental Shelf Research*, *154*, 9–18. https://doi.org/10.1016/j.csr.2018.01.002

Walter, R. K., Reid, E. C., Davis, K. A., Armenta, K. J., Merho, K., & Nidzieko, N. J. (2017). Local diurnal wind-driven variability and upwelling in a small coastal embayment. *Journal of Geophysical Research: Oceans*, *122*, 955–972. https://doi.org/10.1002/2016JC012466

Washburn, L., Fewings, M. R., Melton, C., & Gotschalk, C. (2011). The propagating response of coastal circulation due to wind relaxations along the central California coast. *Journal of Geophysical Research*, *116*, C12028. https://doi.org/10.1029/2011JC007502

Woodson, C. B., Eerkes-Medrano, D. I., Flores-Morales, A., Foley, M. M., Henkel, S. K., Hessing-Lewis, M., et al. (2007). Local diurnal upwelling driven by sea breezes in northern Monterey Bay. *Continental Shelf Research*, *27*(18), 2289–2302. https://doi.org/10.1016/j.csr.2007.05.014